

Hybrid Rydberg-spin qubit of electrons on helium

Erika Kawakami^{1,2,*}, Jiabao Chen³, Mónica Benito⁴, Denis Konstantinov⁵

¹*RIKEN Center for Quantum Computing, RIKEN, Wako, 351-0198, Japan*

²*Cluster for Pioneering Research, RIKEN, Wako, 351-0198, Japan**

³*QunaSys Inc., Bunkyo, Tokyo 113-0001, Japan*

⁴*Institute of Quantum Technologies, German Aerospace Center (DLR),
Wilhelm-Runge-Straße 10, 89081, Ulm, Germany and*

⁵*Quantum Dynamics Unit, Okinawa Institute of Science and
Technology (OIST) Graduate University, Okinawa 904-0495, Japan*

(Dated: March 8, 2023)

We theoretically propose a new way to realize qubits: a hybrid qubit system consisting of the quantized vertical motion (Rydberg states) and the spin states of electrons on the surface of liquid helium. Introducing a local magnetic field gradient hybridizes the Rydberg and spin degrees of freedom, which allows us to benefit from both the long coherence time of the spin state and the long-range Coulomb interaction between electrons that couples the Rydberg state. We present concrete schemes to realize single- and two-qubit gates and quantum-non-demolition read-out. In our framework, the hybridization of the Rydberg state and the spin state is large enough to perform fast qubit gates and small enough not to degrade the coherence time of the spin state significantly, which leads to the realization of high-fidelity qubit gates.

I. INTRODUCTION

Fault-tolerant quantum computing requires a high enough number of interacting qubits placed in two dimensions [1]. Preparing such a system while realizing high-fidelity qubit operations is indispensable. The interest in using electrons in vacuum as qubits has been growing recently. As opposed to using electrons trapped in semiconductor structures, such systems are free of defects or impurities and we can expect long coherence times of their quantum states, which tends to lead to high-fidelity qubit operations. Historically, a single electron was first trapped in vacuum using a Penning trap [2]. Recent efforts on trapping electrons in Paul traps in terms of using them as qubits are reported [3, 4]. A remarkable experimental milestone has been recently achieved using electrons on the surface of solid neon by demonstrating the single-qubit gate operations with 99.95% fidelity [5, 6]. Electrons on the surface of liquid helium is another physical system representing electrons in vacuum. This two-dimensional electron system is known for having the highest measured mobility [7] thanks to the clean interface between liquid helium and vacuum, which suggests the potential for forming a substantial number of uniform qubits. The hydrodynamic instability of liquid can be suppressed for the liquid helium confined in the micro-fabricated devices filled by capillary action [8–13]. Besides the theoretical proposals of using electrons on helium as qubits in early days [14–17], experimental studies on electrons on helium with the aim of using them as qubits are also reported such as trapping a few number of electrons [18], shuttling of the electrons [19], coupling of electrons to microwave (MW) photons via superconducting resonator [20], and coupling of electrons to surface acoustic waves [21]. However, no qubit operations on those electrons have yet been experimentally demonstrated.

A. Rydberg qubit

The initial proposal to realize qubits using electrons on helium focused on the quantized bound states of the electron orbital motion perpendicular to the liquid surface (Rydberg states) [15, 22]. These states of 1D motion in the z direction are formed due to the interaction of an electron with its image charge in liquid helium and have a hydrogen-like energy spectrum. The corresponding eigenfunctions are similar to the radial part of the eigenfunctions in the hydrogen atom, therefore these eigenstates are usually referred to as the Rydberg states, with a typical Rydberg constant on the order 1 meV. The Rydberg-ground state and the Rydberg-1st-excited state are utilized as qubit states. A set of universal single-qubit gates for the Rydberg qubit could be realized by creating an AC electric field whose frequency corresponds to the transition frequency between the two-lowest Rydberg states. The transition frequency can be tuned via the DC Stark shift by a DC electric field E_{\perp} pressing electrons towards the surface. The proposed

* E-mail: e2006k@gmail.com

read-out was to be done destructively by removing the electron in the Rydberg-1st-excited state from the surface and detecting it by an imaging channel plate. A two-qubit gate can be completed via the coupling of qubits by the electric dipole-dipole interaction which arises from the Coulomb interaction between electrons. It utilizes the fact that since an electron's vertical position depends on the Rydberg state, so does the strength of the electric dipole-dipole interaction. This is a unique feature of electrons on cryogenic substrates such as liquid helium, solid neon and solid hydrogen [5, 23]. Compared to the electrons on cryogenic substrates, the Coulomb interaction is reduced in semiconductors since the relative electric permittivity in Si and GaAs is typically $\epsilon_r \approx 12$. Additionally, the electrons are more tightly confined normal to the interface. Consequently, the electrons' positions, and thus the strength of the electric dipole-dipole interaction, depend little on the vertical quantum state in semiconductors. As shown below, the electric dipole-dipole interaction energy stays as large as $4J/h \approx 140$ MHz for electrons on helium even if two qubits are separated by a distance as far as $d = 0.88 \mu\text{m}$. This fact indicates that qubits can interact with each other without having any additional structures such as a floating gate [24] or a superconducting resonator [5, 20, 25], ergo reducing the complexity of the qubit architecture. Ref. [15, 22] theoretically showed that a metallic pillar can trap a single electron. Cutting-edge nanofabrication techniques allow us to wire pillars every $0.88 \mu\text{m}$ [26]. However, in order to cancel out the unintended state-evolution caused by this always-on electric dipole-dipole interaction, one should continuously apply a decoupling sequence [27], which would add complications when realizing quantum gates. Another disadvantage of using the Rydberg state is its relatively short relaxation time ($T_1 \sim 1\mu\text{s}$) [28, 29].

B. Spin qubit

It was pointed out that the spin states of the electrons on liquid helium are expected to have an extremely long coherence time > 100 s, and therefore were proposed to be used as qubit states [16]. Later, Schuster et al. proposed to couple the MW photons and the orbital motion parallel to the liquid surface (hereafter, we refer to the parallel orbital motion as the orbital state, while the perpendicular orbital motion is called the Rydberg state) via a superconducting resonator [17]. There, an external magnetic field is applied parallel to the liquid surface and the orbital and spin degrees of freedom can be coupled due to a local magnetic field gradient created by a current running through a wire underneath the electron. In this way, the spin qubit can be read out and different spin qubits can be coupled via the superconducting resonator. Alternatively, the spin states of adjacent electrons can interact with each other via the coupling of the spin state of each electron to a normal mode of the collective in-plane vibration of the electrons arising due to the Coulomb interaction [30, 31]. One concern about this operation scheme is a strong enhancement of the spin relaxation rate. To be fast, both single-qubit and two-qubit gates require a small energy detuning between the spin-up orbital-ground state and the spin-down orbital-1st-excited state. However, this opens a path for quasi-elastic spin-orbit-flip process induced by an absorption or emission of a single ripplon, a quantum of surface capillary waves, thus significantly increasing the spin relaxation rate. For the considered detuning 5 MHz, the spin relaxation rate was estimated to be 0.6×10^3 and $6 \times 10^5 \text{ s}^{-1}$ for the pressing field $E_{\perp} = 0$ and 300 V/cm , respectively [30].

C. Hybrid Rydberg-Spin qubit

Here, we propose a hybrid qubit comprising the Rydberg state and the spin state. A magnetic field gradient created by a nanofabricated ferromagnet introduces the interaction between the Rydberg and spin degrees of freedom (Rydberg-spin interaction) and the interaction between the orbital and spin degrees of freedom (spin-orbit interaction). The long coherence time of the spin state is essential to realize high-fidelity qubit operations, while the long-range Coulomb interaction affecting the Rydberg states allows us to place electrons at a moderate distance while keeping a considerable interaction between them, which is a basic requirement for realizing a high number of qubits in a two-dimensional array. A detailed device geometry and measurement schemes are presented in Sec. II and the Hamiltonian of the system is presented in Sec. III. The spin-orbit interaction allows us to realize a set of universal single-qubit gates for the spin state with excitation by an AC electric field in an electric-dipole-spin-resonance (EDSR) manner [32], which is presented in Sec. IV. The Rydberg-spin interaction allows us to excite the Rydberg state spin-selectively. Sec. VII shows that we can realize a controlled-phase gate for the spin state by a sequence of spin-selective Rydberg-transitions with the assistance of the intrinsic electric dipole-dipole interaction. Moreover, a quantum-non-demolition (QND) readout of the spin state can be accomplished by detecting the spin-selective Rydberg-transition using an LC circuit, which is presented in Sec. VIII.

When single-qubit gates are performed and calculation is idle, the qubit states are always in the Rydberg-ground state therefore we do not directly suffer from the fast relaxation of the Rydberg state. However, the introduced spin-orbit interaction and Rydberg-spin interaction open a path for the spin state to relax or dephase via the relaxation or the dephasing of the orbital state and the Rydberg state. The details of the calculation of the spin relaxation and

dephasing rates are presented in Sec. V and Sec. VI, respectively. Similar to Ref. [30], we identify the spin relaxation as the major source of the spin decoherence. However, different from Ref. [30], for a typical energy spectrum of a trapped electron in a perpendicular magnetic field considered in this proposal, we have a substantial energy difference between the spin-up orbital-ground state and the spin-down orbital-1st-excited state. This allows us to eliminate the spin-orbit flips due to fast quasi-elastic one-rippion processes, leaving a much slower two-rippion emission as a major source of spin relaxation. Below, we estimate the spin relaxation rate ~ 10 s⁻¹ for a typical pressing field experienced by the electron $E_{\perp} = 200$ V/cm. Thanks to a higher magnetic field gradient than in Ref. [30], we can have fast enough single-qubit gates and two-qubit gates even if the spin-up orbital-ground state and the spin-down orbital-1st-excited state are highly detuned.

II. PHYSICAL REALIZATION OF THE HYBRID RYDBERG-SPIN QUBIT

We propose to fabricate a pillar (center electrode) and segmented toroidal electrodes (outer electrodes) and to trap a single electron on top of the pillar (Fig. 1(a)). For electrons on helium, it is well known that electrons freeze into a Wigner crystal when the Coulomb energy $e^2/d \sim 10$ K (with $d = 0.88\mu\text{m}$) exceeds the kinetic energy $k_B T$ [33]. By patterning pillars into a triangular lattice, we can avoid having incommensurability between the lattice formed by the pillars and the Wigner lattice formed by the Coulomb interaction. This allows us to perform topological quantum error correction for qubits in a triangular lattice [34]. The adjacent pillars are separated by $d = 0.88 \mu\text{m}$ (Fig. 1(d)) and so are the electrons trapped by them, which allows us to prepare $> 10^7$ qubits in the area of 1 cm^2 . The intrinsic Rydberg-spin interaction is zero. Here, we introduce an artificial one via a local magnetic field gradient which is created by making a pillar of a ferromagnetic material (cobalt) [32, 35] (Fig. 1(a)). Different from Ref. [17, 30], we propose to apply an external magnetic field normal to the liquid helium surface. The stray magnetic fields are created by the ferromagnet at the position of the Rydberg-ground state and the Rydberg-1st excited state, which are presented in Fig. 1(b) and in Fig. 1(c), respectively. The created magnetic field gradient introduces both the Rydberg-spin interaction and the spin-orbit interaction.

It is indispensable to demonstrate how to realize qubit operations such as single-qubit gates, a two-qubit gate, read-out, and initialization. The spin-orbit interaction makes it possible to realize a universal set of single-qubit gates in an EDSR manner [32] by applying an AC voltage $\propto \cos(\omega_{\text{EDSR}}t)$ to one of the outer electrodes (Fig. 1) with $\omega_{\text{EDSR}}/2\pi = 16$ GHz corresponding to the Zeeman splitting for the Rydberg-ground state under 1.75 T magnetic field. This magnetic field is high enough to stabilize the magnetization of cobalt [36] and this MW frequency is low enough to have a reasonably small attenuation through coaxial cables. In the course of a two-qubit gate, a transition between the Rydberg-ground state and the Rydberg-1st-excited state is required. Such a transition can be realized by applying a MW signal $\propto \cos(\omega_{\text{MW}}t)$ with $\omega_{\text{MW}}/2\pi \sim 240$ GHz through a waveguide (Fig. 1(d)). The transition energy can be tuned by DC voltages applied to the center electrode and the outer electrodes, V_1 and V_2 , respectively (Fig. 1(a)), via the DC Stark shift (Fig. S2). Thus, by applying different voltages for different qubits, individual qubits can be addressed. The spin-spin interaction can be mediated by exciting the Rydberg state spin-selectively via the Rydberg-spin interaction, which allows us to realize a two-qubit gate for the qubit state. As for the read-out and initialization, we propose to read out the excitation of the Rydberg state of the electrons capacitively through the center electrode underneath the electron. When the electron is excited from the Rydberg-ground state to the Rydberg-1st-excited state, the electron changes its position vertically and the image charge induced on the center electrode changes (Fig. 1(b,c)). An LC-resonant circuit can be formed by an inductance connected to the center electrode and the parasitic capacitance. The image charge change induced on the center electrode can be detected by the shift in the resonance frequency of the LC circuit. An RF signal $\cos(\omega_m t)$ set to near the resonance frequency (~ 100 MHz) is sent to the center electrode and the reflected signal is measured. We show that the sensitivity of the method is sufficient to detect the Rydberg excitation of a single electron. This detection technique is analogous to the gate-based read-out in semiconductor quantum dots [37] and the single-electron detection in Penning traps [2]. We have also recently demonstrated this detection technique for many electrons on liquid helium [11, 38]. Thanks to the Rydberg-spin interaction, detection of the Rydberg excitation is transformed into the spin read-out of a single electron and is feasible using an LC circuit. This detection works as a QND measurement for the qubit state as demanded for a large-scale quantum computation with quantum error correction.

III. HAMILTONIAN OF THE SYSTEM

A static magnetic field $\mathbf{B}_0 = B_0 \mathbf{e}_z$ is applied normal to the helium surface, and therefore the electron is trapped both magnetically and electrically. Using the cylindrical coordinates with the (r, θ) plane parallel to the liquid surface, the electric potential felt by the electron and the orbital wavefunction can be written as $V(r, z)$ and $\Phi(r, z, \theta) =$

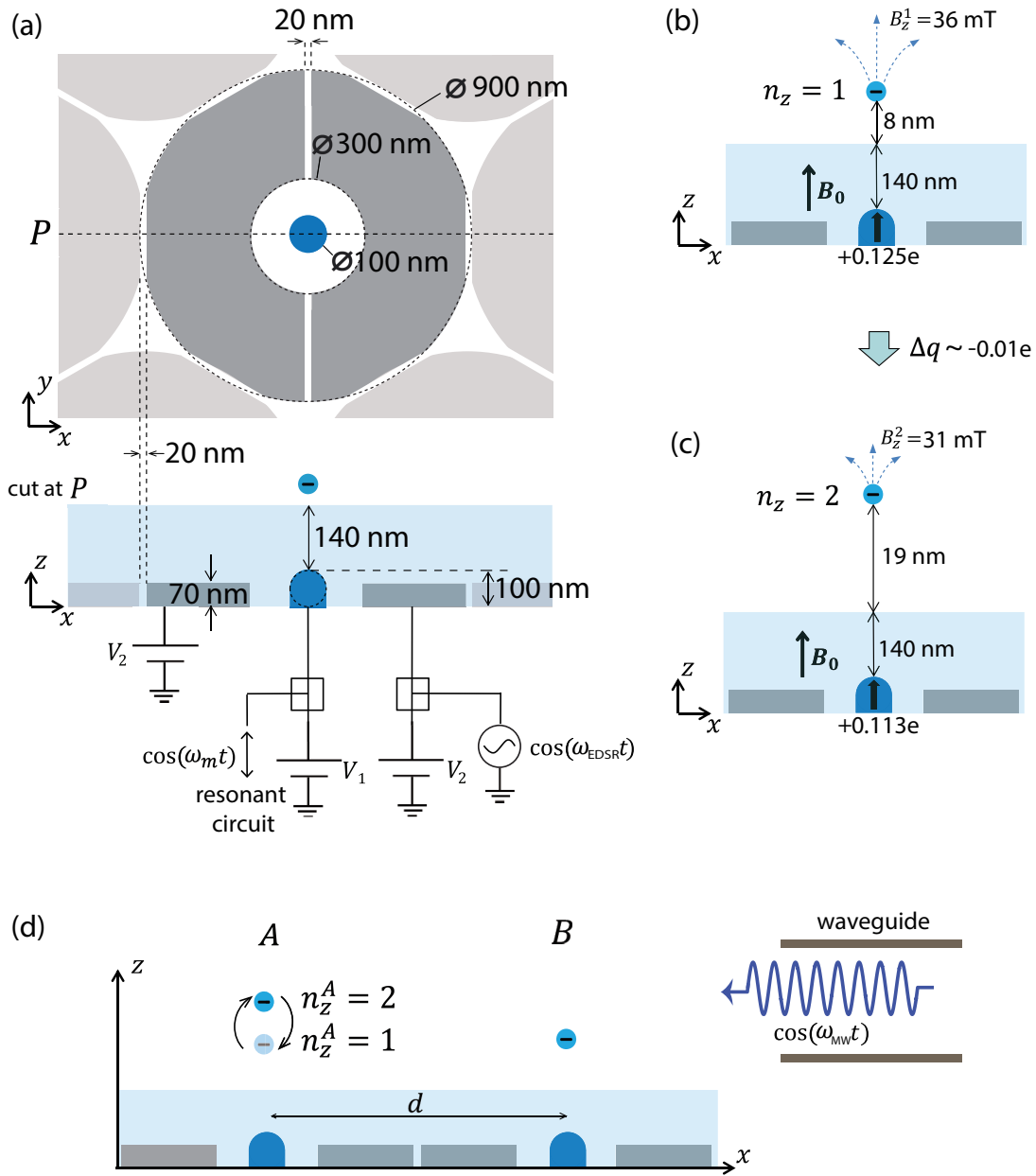


FIG. 1. (a) A ferromagnetic pillar (center electrode) is shown in blue and the segmented toroidal electrodes (outer electrodes) are shown in gray. A single electron is trapped on top of the center electrode. The outer electrodes for the neighboring electrons are shown in light gray. The gap between the outer electrodes is 20 nm. The thickness of liquid ^4He (light blue) above the center electrode is set to 140 nm. The center electrode forms a 100 nm diameter pillar, the tip of which is rounded. V_1 and V_2 are the voltages applied to the center electrode and the two outer electrodes, respectively. (b,c) An external magnetic field B_0 is applied along the z axis. Under a sufficiently high B_0 (> 100 mT for cobalt [25]), the pillar is magnetized along the same axis. When $V_1 = 60$ mV and $V_2 = -45$ mV, the average position of the electron along the z axis is 8 nm and 19 nm from the helium surface for the Rydberg-ground state ($n_z = 1$) in (b) and for the Rydberg-1st-excited state ($n_z = 2$) in (c), respectively (see also Fig. S1). The image charge induced on the center electrode is $0.125e$ and $0.113e$ for $n_z = 1$ and $n_z = 2$, respectively. The field lines of the stray magnetic field are shown at position of electron for $n_z = 1$ (for $n_z = 2$) in (b) (in (c)). B_z^1 (B_z^2) is the z component of the stray magnetic field felt by the electron in the Rydberg-ground (Rydberg-1st-excited) state. (d) Two neighboring electrons A and B are separated by $d = 0.88 \mu\text{m}$ and are used as qubit A and qubit B, respectively. In the case shown here, electron A's Rydberg transition is on resonance with the MW applied through a waveguide. Electron A goes back and forth between the Rydberg-ground state ($n_z^A = 1$) and the Rydberg-1st-excited state ($n_z^A = 2$) (see texts for details).

$\phi_{m,n_r,n_z}(r,z)\psi_m(\theta)$, respectively, since both the DC electric and magnetic potentials are approximately azimuthally symmetric (see Sec. S1 of the supplementary information for more details). Using the symmetric gauge, the vector

potential reads $\mathbf{A} = \frac{B_0 \mathbf{e}_z \times \mathbf{r}}{2} = \left(-\frac{B_0 y}{2}, \frac{B_0 x}{2}, 0\right)$. The Schrödinger equation of the system is written as (see Sec. S1 of the supplementary information for more details)

$$H_0 \phi_{m,n_r,n_z}(r,z) = E_{m,n_r,n_z}^{(0)} \phi_{m,n_r,n_z}(r,z), \quad (1)$$

with

$$H_0 = -\frac{\hbar^2}{2m_e} \left(\frac{1}{r} \frac{\partial}{\partial r} + \frac{\partial^2}{\partial r^2} + \frac{\partial^2}{\partial z^2} - \frac{m^2}{r^2} \right) + \frac{1}{2} \hbar \omega_c m + \frac{1}{8} m_e \omega_c^2 r^2 - eV(r,z), \quad (2)$$

and $\psi_m(\theta) = \frac{1}{\sqrt{2\pi}} e^{Im\theta}$, where $I^2 = -1$, $m = 0, \pm 1, \pm 2, \pm 3, \dots$, $\omega_c = eB_0/m_e$ is the cyclotron frequency, m_e is the electron mass, and $e > 0$ is the elementary charge. We numerically solved Eq. (S4) to obtain the normalized eigenfunctions $\phi_{m,n_r,n_z}(r,z)$ and the energy eigenvalues, which are shown in Fig. S1 of the supplementary material. We associate the Rydberg-energy levels with $n_z = 1, 2, 3, \dots$ and the orbital energy levels with $n_r = 0, 1, 2, 3, \dots$ (see the supplementary information for more details). With increasing V_1 , both the Rydberg transition energy and the orbital transition energy become higher (both the confinement along the z axis and the confinement along the x, y axes become stronger). With decreasing V_2 , the Rydberg transition energy becomes lower, while the orbital transition energy becomes larger (see Fig. S2). It is preferable to have higher orbital transition energies to suppress the relaxation rate and the spin dephasing rate. If the Rydberg transition energy becomes too high, it is not straightforward to send a resonant MW of high enough power and the MW multiplier becomes expensive [39]. In order to send a high enough power with relatively inexpensive equipment (WR4 waveguides and multiplier [39]), we aim to keep the Rydberg transition energy less than ≈ 240 GHz. For this reason, hereafter, we consider the case where $V_1 = 60$ mV and $V_2 = -45$ mV, such that the Rydberg transition energy is ≈ 240 GHz (see Fig. S2). The vertical and in-plane stray magnetic fields created by the ferromagnetic pillar near the position of the electron in the Rydberg-ground state can be approximately described as $b_z(r,z) = B_z^1 + \frac{\partial b_z}{\partial z}(z - z_{11}) + \frac{\partial^2 b_z}{\partial r^2} r^2$ and $b_r(r,z) = \frac{\partial b_r}{\partial r} r$, respectively. $z_{n_z n'_z}$ stands for $\langle \phi_{m=0,n_r=0,n_z} | z | \phi_{m=0,n_r=0,n'_z} \rangle$ and therefore z_{11} is the average position of the electron in the Rydberg-ground state. B_z^1 and $\frac{\partial b_z}{\partial z}$, $\frac{\partial^2 b_z}{\partial r^2}$, and $\frac{\partial b_r}{\partial r}$ are the z component of the stray field and the field gradients at $(r,z) = (0, z_{11})$, respectively. To account for the effect of the ferromagnetic pillar, we rewrite the Hamiltonian as $H = H_0 + W$, where H_0 is given by Eq. (S5) with $\omega_c = eB/m_e$, $B = B_0 + B_z^1$, and $W = W_z + W_r$ is the Hamiltonian of the Rydberg-spin interaction with

$$W_z = \frac{1}{2} g \mu_B \left(\frac{\partial b_z}{\partial z} (z - z_{11}) + \frac{\partial^2 b_z}{\partial r^2} r^2 \right) \sigma_z, \quad (3)$$

and

$$W_r = \frac{1}{2} g \mu_B \frac{\partial b_r}{\partial r} r \sigma_r. \quad (4)$$

Here, σ_{\square} with $\square = x, y, z$ are Pauli matrices spanned by the spin-up and spin-down states, $\sigma_r = \sigma_x \cos \theta + \sigma_y \sin \theta$, g is the free electron Lande g factor, and μ_B is the Bohr magneton. Fig. 2 (a) and (b) show b_r and b_z , respectively, as a function of r at $z = z_{11}$.

IV. UNIVERSAL SET OF SINGLE-QUBIT GATES

Single-qubit gates for the spin state can be realized by applying an AC voltage to one of the two outer electrodes and thus creating an AC electric field along the x axis at the position of the electron with the corresponding Hamiltonian for the electron interaction with the electric field $V^{\text{EDSR}}(t) = U e^{-i\omega_{\text{EDSR}} t} + U^\dagger e^{i\omega_{\text{EDSR}} t}$, where $U = eE^{\text{EDSR}} x/2$ and $\omega_{\text{EDSR}} = g\mu_B B/\hbar$ (Fig. 1(a)). This electric field interacts with the orbital degree of freedom and due to the spin-orbit interaction created by the in-plane field gradient, with the corresponding Hamiltonian W_r , we can control the spin state coherently in an EDSR manner [32]. The part of the Hamiltonian which is responsible for the coherent control of the spin state is given by

$$H(t) = V^{\text{EDSR}}(t) + W_r. \quad (5)$$

Here, we take H_0 in Eq. (S5) with $\omega_c = eB/m_e$ as the unperturbed term and treat $H(t)$ in Eq. (S7) as the perturbation term. The spin-flip transition happens due to virtual transitions of an electron to excited orbital states, and according to the Fermi's golden rule in the second-order perturbation theory, the transition rate is approximately given by

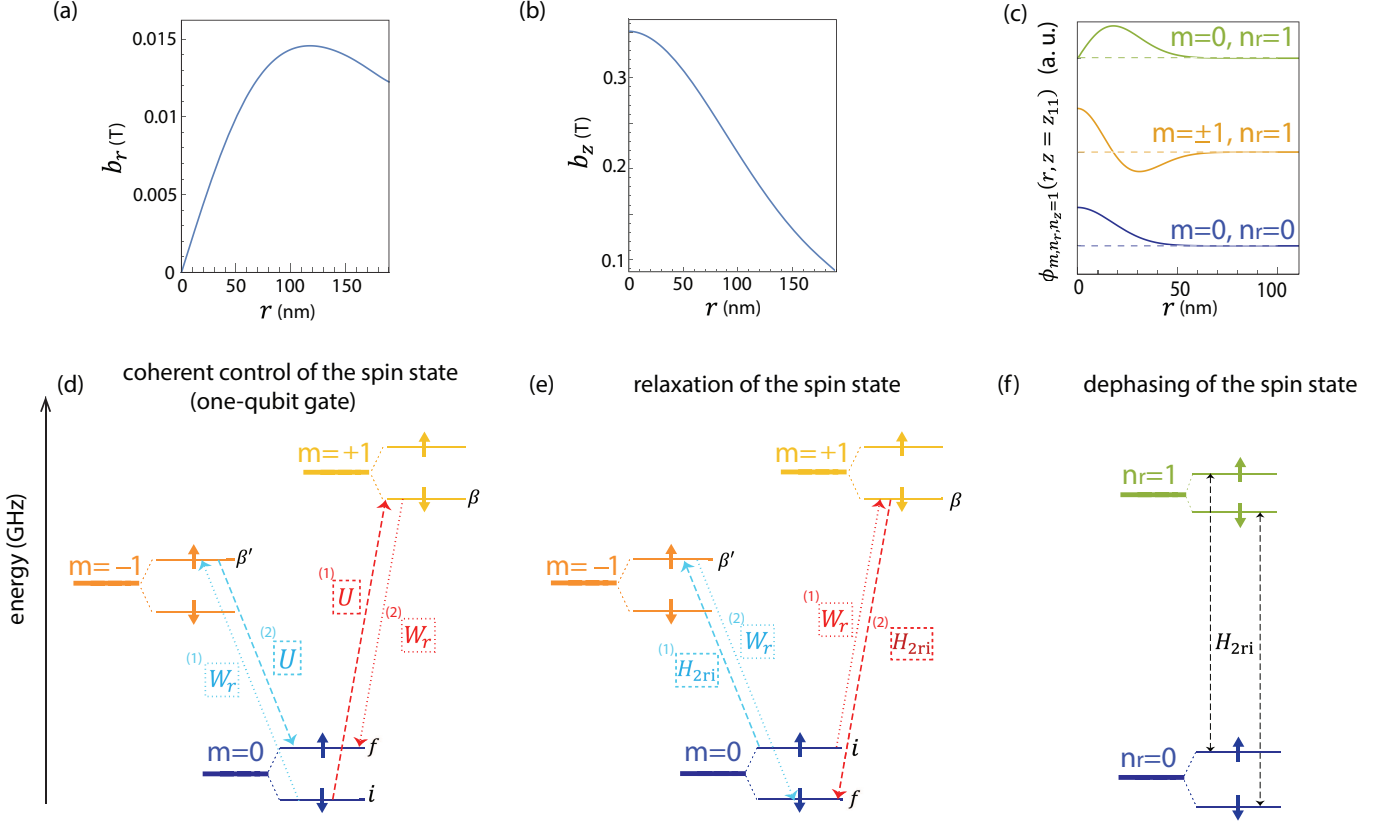


FIG. 2. (a,b) The r component of the stray magnetic field (b_r) and the z component of the stray magnetic field (b_z) created by the ferromagnetic pillar as a function of r at $z = z_{11}$ for the saturation magnetization of Co (1.8 T). (c) The wavefunction along r for the $m = 0$, $n_r = 0$, and $n_z = 1$ state (blue), for the $m = \pm 1$, $n_r = 1$, and $n_z = 1$ state (yellow), and the $m = 0$ and $n_r = 1$ state (green). The dashed lines are the offsets for clarity. (d,e) Cartoon figure of the energy levels for $n_r = 0$, $n_z = 1$, and $m = 0, \pm 1$ states. i and f stand for the initial and final states, respectively, and β and β' stand for the intermediate state of the second-order process. (d) The process of the coherent control of the spin state. The virtual transition with simultaneous flipping of the orbital state and the spin state (dotted arrows) can be caused due to the in-plane field gradient, with the corresponding Hamiltonian W_r . Dashed arrows represent the virtual transitions induced by the AC electric field with the corresponding Hamiltonian U . As a result, the spin state is flipped for $m = 0$ in the end. (e) The process of the relaxation of the spin state. As in (d), the simultaneous flipping of the orbital state and the spin state (dotted arrows) happens due to the in-plane field gradient with the corresponding Hamiltonian W_r . Different from (d), the transitions between the orbital states (dashed arrows) are induced by the two-ripplon scattering with the corresponding Hamiltonian H_{2ri} . (f) Cartoon figure of the energy levels for $m = 0$, $n_z = 1$, and $n_r = 0, 1$ states. The electron experiences different magnetic fields depending on whether it is in $n_r = 0$ state or $n_r = 1$ state (see (b,c)).

$$\Gamma_{\text{EDSR}} = \frac{2\pi}{\hbar} \left| \frac{(W_r)_{f\beta}(U)_{\beta i}}{E_i - E_\beta + \hbar\omega_{\text{EDSR}}} + \frac{(U)_{f\beta'}(W_r)_{\beta' i}}{E_i - E_{\beta'}} \right|^2 \delta(E_f - E_i - \hbar\omega_{\text{EDSR}}), \quad (6)$$

where $i = (m = 0, \downarrow)$, $f = (m = 0, \uparrow)$, $\beta = (m = +1, \downarrow)$, $\beta' = (m = -1, \uparrow)$, and $(W_r)_{f\beta}$ stands for $\langle f | W_r | \beta \rangle$. E_\square stands for the electron energy of the state $\square = (m, n_r, n_z, \sigma)$, where $E_{m, n_r, n_z, \sigma} = E_{m, n_r, n_z}^{(0)} + \frac{1}{2}g\mu_B B\sigma$ and σ represents the spin-up state ($\sigma = \uparrow$ or $+1$) or the spin-down state ($\sigma = \downarrow$ or -1). We omit some indexes for clarity when the electron is in the ground state for those quantum numbers. Note that the virtual spin-flip transitions induced by W_r require a change in the orbital magnetic number m by ± 1 . Here, we take into account only the transitions between the states with $n_r = 0$ and $n_z = 1$. The contributions from the higher states are much smaller, and thus are neglected. The first (second) term in $|\dots|^2$ of Eq. (6) corresponds to the transition process shown with red (light blue) arrows in Fig. 2(d). From this, we obtain the Rabi frequency, $f_{\text{Rabi}} = \frac{1}{8}\partial_r f_{b_r} \partial_x f_{\text{AC}} l_0^2 \left| \frac{1}{f_i - f_\beta + f_{\text{EDSR}}} + \frac{1}{f_i - f_{\beta'}} \right|$, where $l_0 = |\langle \phi_{m=0, n_r=0, n_z=1} | r | \phi_{m=\pm 1, n_r=0, n_z=1} \rangle|$, $\partial_r f_{b_r} = g\mu_B \frac{\partial b_r}{\partial r} / \hbar$, $\partial_x f_{\text{AC}} = eE^{\text{EDSR}} / \hbar$, $f_\square = E_\square / \hbar$ for $\square = i, \beta, \beta'$ and $f_{\text{EDSR}} = \omega_{\text{EDSR}} / 2\pi$. Our numerical simulation shows that the in-plane magnetic field gradient is $\frac{\partial b_r}{\partial r} = 0.23$ mT/nm

when the cobalt pillar is fully magnetized along the z axis after reaching its saturation magnetization (1.8 T). With $V_1 = 60$ mV, $V_2 = -45$ mV, $\omega_{\text{EDSR}} \approx \omega_c = 16$ GHz, and the strength of the electric field at the position of the electron, $E^{\text{EDSR}} = 500$ V/cm, the Rabi frequency is calculated to be $f_{\text{Rabi}} \approx 100$ MHz (Fig. S3). We also find that the Rabi frequency gets higher when the orbital confinement gets weaker as the coupling strength between the spin state and the orbital state becomes larger. $E^{\text{EDSR}} = 500$ V/cm can be realized by applying an AC voltage to one of the outer electrodes (Fig. 1b) with an amplitude $E^{\text{EDSR}}/\alpha = 12.5$ mV, which is small enough not to cause significant heating problem experimentally. From a COMSOL simulation, the conversion factor is calculated to be $\alpha \approx 4 \times 10^6$ m $^{-1}$. Since single-qubit gates are performed by sending an AC voltage to each electrode allocated to each qubit, qubits can be individually addressed. The universal set of single-qubit gates can be realized by adjusting the phase of the AC voltage. The single-qubit gate fidelity is determined by $f_{\text{Rabi}} \approx 100$ MHz and the spin relaxation rate $\Gamma_{\text{relaxation}} \approx 50$ ms (see Sec. V) and it is calculated to be $> 99.9999\%$ (see the supplementary information for more details).

V. SPIN RELAXATION

While the in-plane field gradient $\frac{\partial b_r}{\partial r}$ allows us to realize single-qubit gates, it also opens the path for the spin-up state to relax to the spin-down state. Such relaxation is induced by the virtual transitions between electron orbital states that happen due to the interaction between the electron and the liquid helium surface capillary waves called ripples (Fig. 2(e)). The spin relaxation is the energy non-conserving process and is dominated by the emission of two short-wavelength ripples [40] (see the supplementary information for more details). The Hamiltonian of the electron-ripple interaction, which corresponds to the two-ripple processes, is quadratic in surface displacement and is given by $H_{2\text{ri}} = \sum_{\mathbf{q}_1} \sum_{\mathbf{q}_2} \xi_{\mathbf{q}_1} \xi_{\mathbf{q}_2} U_{\mathbf{q}_1 \mathbf{q}_2} e^{i\mathbf{q}_1 \mathbf{r}} e^{i\mathbf{q}_2 \mathbf{r}}$, where $\xi_{\mathbf{q}} = Q_{\mathbf{q}}(a_{\mathbf{q}} + a_{-\mathbf{q}}^\dagger)$ is the Fourier transform of the operator of the surface displacement of liquid helium, $a_{\mathbf{q}}$ and $a_{-\mathbf{q}}$ are the creation and annihilation operators for ripples, respectively, $Q_{\mathbf{q}} = \sqrt{\frac{\hbar q}{2S\rho\omega_{\mathbf{q}}}}$, S is the surface area of the liquid and ρ is the density of liquid helium. $U_{\mathbf{q}_1 \mathbf{q}_2}$ is the electron-two-ripple coupling (see the supplementary information for more details). Here, we take $H_{2\text{ri}} + W_r$ as the perturbation term and the other Hamiltonian terms that are responsible for the spin relaxation as the unperturbed term. According to the Fermi's golden rule in the second-order perturbation theory, the relaxation rate is approximately given by

$$\Gamma_{\text{relaxation}} = \frac{2\pi}{\hbar} \left| \frac{(W_r)_{f\beta'} (H_{2\text{ri}})_{\beta'i}}{E_i - E_{\beta'} + \epsilon_{n_{\text{ri}}} - \epsilon_{n'_{\text{ri}}}} + \frac{(H_{2\text{ri}})_{f\beta} (W_r)_{\beta i}}{E_i - E_{\beta}} \right|^2 \delta(E_f - E_i + \epsilon_{n'_{\text{ri}}} - \epsilon_{n_{\text{ri}}}), \quad (7)$$

where $\epsilon_{n_{\text{ri}}}$ and $\epsilon_{n'_{\text{ri}}}$ are the energies of the collective states of the ripples before and after the two-ripple emission, respectively, and therefore $\epsilon_{n'_{\text{ri}}} - \epsilon_{n_{\text{ri}}} = \hbar\omega_{\mathbf{q}_1} + \hbar\omega_{\mathbf{q}_2}$, where $\hbar\omega_{\mathbf{q}_1}$ and $\hbar\omega_{\mathbf{q}_2}$ are the energies of the emitted ripples [15]. With $V_1 = 60$ mV, $V_2 = -45$ mV, $\omega_{\text{EDSR}} \approx \omega_c = 16$ GHz, the relaxation time $1/\Gamma_{\text{relaxation}}$ is calculated to be ≈ 50 ms (Fig. S4). We also find that the relaxation rate has the tendency to increase when the orbital confinement gets weaker (see the supplementary information for more details).

VI. SPIN DEPHASING

The dephasing of the spin state happens due to the fluctuation of the Zeeman splitting over time. Such a fluctuation is induced by spin-conserving virtual transitions of an electron to higher orbital states which experience different magnetic fields. Here, the virtual orbital transitions between $n_r = 0$ to $n_r = 1$ states induced by the two-ripple scattering of the thermally excited long-wavelength ripples is a dominant process, which is illustrated in Fig. 2(f) (see the supplementary information for more details). We take into account only $n_z = 1$. The contributions from the virtual transitions to $n_z > 1$ states are much smaller, and thus are neglected. The virtual transitions to $m \neq 0$ states are forbidden because of the conservation of the electron angular momentum. As seen from the spread of the wavefunction shown in Fig. 2(c) and the r dependence of the stray magnetic field in Fig. 2(b), the electron experiences different quantizing magnetic fields depending on whether it is in the state $n_r = 0$ or $n_r = 1$. Hence the orbital transition leads to the dephasing. Similar to the dephasing of the Rydberg states introduced in [15], the dephasing time of the spin state D_{φ}^{-1} is related to the auto-correlation function of the time-dependent energy level splitting between the spin-up state and the spin-down state $\delta E(t)$: $\langle \delta E(t') \delta E(t'') \rangle = \hbar^2 D_{\varphi} \delta(t' - t'')$, where $\delta(t)$ is Dirac delta function. Different from the single-qubit gates and the spin relaxation, here the in-plane field gradient $\frac{\partial^2 b_z}{\partial r^2}$ is responsible for the spin dephasing and thereby we take $H_{2\text{ri}} + W_z$ as the perturbation term. The time-dependent

energy is calculated as the second-order energy shift caused by the perturbation term:

$$\delta E(t) = \frac{2 \langle \phi_{n_r=0} | H_{2ri} | \phi_{n_r=1} \rangle (\langle \phi_{n_r=1, \uparrow} | W_z | \phi_{n_r=0, \uparrow} \rangle - \langle \phi_{n_r=1, \downarrow} | W_z | \phi_{n_r=0, \downarrow} \rangle)}{E_{n_r=0} - E_{n_r=1}}. \quad (8)$$

With $V_1 = 60$ mV, $V_2 = -45$ mV, $\omega_{\text{EDSR}} \approx \omega_c = 16$ GHz, and the liquid helium temperature $T = 100$ mK, the spin dephasing time D_φ^{-1} is calculated to be ≈ 100 s (Fig. S5). As the process is dominated by the thermally excited ripplons, the dephasing time becomes even longer as the liquid helium temperature is lowered (Fig. S5(c)). This dephasing time is much longer than the relaxation time calculated in Sec. V and thus the coherence time is determined by the relaxation time.

VII. TWO-QUBIT GATE

A two-qubit gate for the spin state can be realized by exciting the Rydberg state spin-selectively and depending on the Rydberg state of an adjacent electron. In Sec. VII A, we show that the Rydberg transition energy of an electron depends on the spin state of the electron itself and the Rydberg state of an adjacent electron. In Sec. VII B, a concrete MW pulse sequence to realize a controlled-phase gate is presented.

A. Perturbation due to the electric dipole-dipole interaction

Besides perturbation caused by the stray magnetic field gradient, when two electrons are close enough, we should consider perturbation caused by the electric dipole-dipole interaction. It is induced by the fact that the strength of the Coulomb interaction depends on the distance between the average positions of electrons, which depends on whether they are in the same Rydberg state. In the two-lowest level approximation, taking the Rydberg-ground state $|n_z = 1\rangle$ and the Rydberg-1st-excited state $|n_z = 2\rangle$ as basis states, the Hamiltonian of the electric dipole-dipole interaction can be expressed as

$$W' = \frac{e^2}{4\pi\epsilon_0 d^3} \left((z_{11}^A - z_{22}^A)(z_{11}^B - z_{22}^B) \frac{s_z^A s_z^B}{4} + 2z_{12}^A z_{12}^B \frac{s_x^A s_x^B + s_y^A s_y^B}{4} \right), \quad (9)$$

where $s_z^i = |n_z^i = 2\rangle \langle n_z^i = 2| - |n_z^i = 1\rangle \langle n_z^i = 1|$, $s_x^i = |x+\rangle \langle x+| - |x-\rangle \langle x-|$, $s_y^i = |y+\rangle \langle y+| - |y-\rangle \langle y-|$, $|x\pm\rangle = \frac{1}{\sqrt{2}}(|n_z^i = 2\rangle \pm |n_z^i = 1\rangle)$, and $|y\pm\rangle = \frac{1}{\sqrt{2}}(|n_z^i = 2\rangle \pm I |n_z^i = 1\rangle)$ for qubit A ($i = A$) or qubit B ($i = B$) [15]. ϵ_0 is the vacuum permittivity and d is the in-plane distance between pillars. Treating W' as the perturbation term, the first-order energy shift for the two-lowest Rydberg states ($n_z^i = 1, 2$) is given by

$$\langle n_z^A | \langle n_z^B | W' | n_z^A \rangle | n_z^B \rangle \approx J(-1)^{n_z^A} (-1)^{n_z^B}. \quad (10)$$

The interaction energy is $4J = \kappa \frac{e^2}{4\pi\epsilon_0} \frac{(z_{11}^A - z_{22}^A)(z_{11}^B - z_{22}^B)}{d^3}$, where κ is the factor acquired due to the screening effect (see Sec. S.VI.A of the supplementary information). The Zeeman energy for the Rydberg-ground state is larger than that for the Rydberg-1st-excited state by $\Delta b = g\mu_B |\Delta B_z|$, with $\Delta B_z = B_z^2 - B_z^1$ (Fig. 1(b,c)). In the same way, the Rydberg transition energy also differs by Δb depending on the spin state (Fig. 3(a)). Note that the external magnetic field is much larger than the stray magnetic field and thus only the magnetic field along the quantization axis (the z axis) is considered. In total, the first-order energy shift of the two-electron system caused by both the Coulomb interaction and the magnetic field gradient is

$$\sum_{i=A,B} \frac{1}{2} \Delta b (1 - n_z^i) \sigma^i + J(-1)^{n_z^A} (-1)^{n_z^B}. \quad (11)$$

As a result, the energy for the transition between the Rydberg-ground state and the Rydberg-1st-excited state of qubit A (B) depends on the Rydberg state of qubit B (A) and the spin state of qubit A (B) (Fig. 3(a)). Here, the energy shift due to the magnetic dipole-dipole interaction, which is much smaller than the terms in Eq. (11), is neglected. The energy shift due to the band-like structure when qubits are placed in a triangular array is also negligibly small when the distance between neighboring electrons is much larger than the distance between the electron and the electrode underneath it [15]. With $d = 0.88$ μm and $z_{11}^A - z_{22}^A = z_{11}^B - z_{22}^B = 11.5$ nm, we obtain $4J = 137$ MHz and $\Delta b = g\mu_B |\Delta B_z| \approx 4J$ with $\Delta B_z \approx -5$ mT (Fig. 1(b,c)).

B. Pulse sequence for a CPhase gate

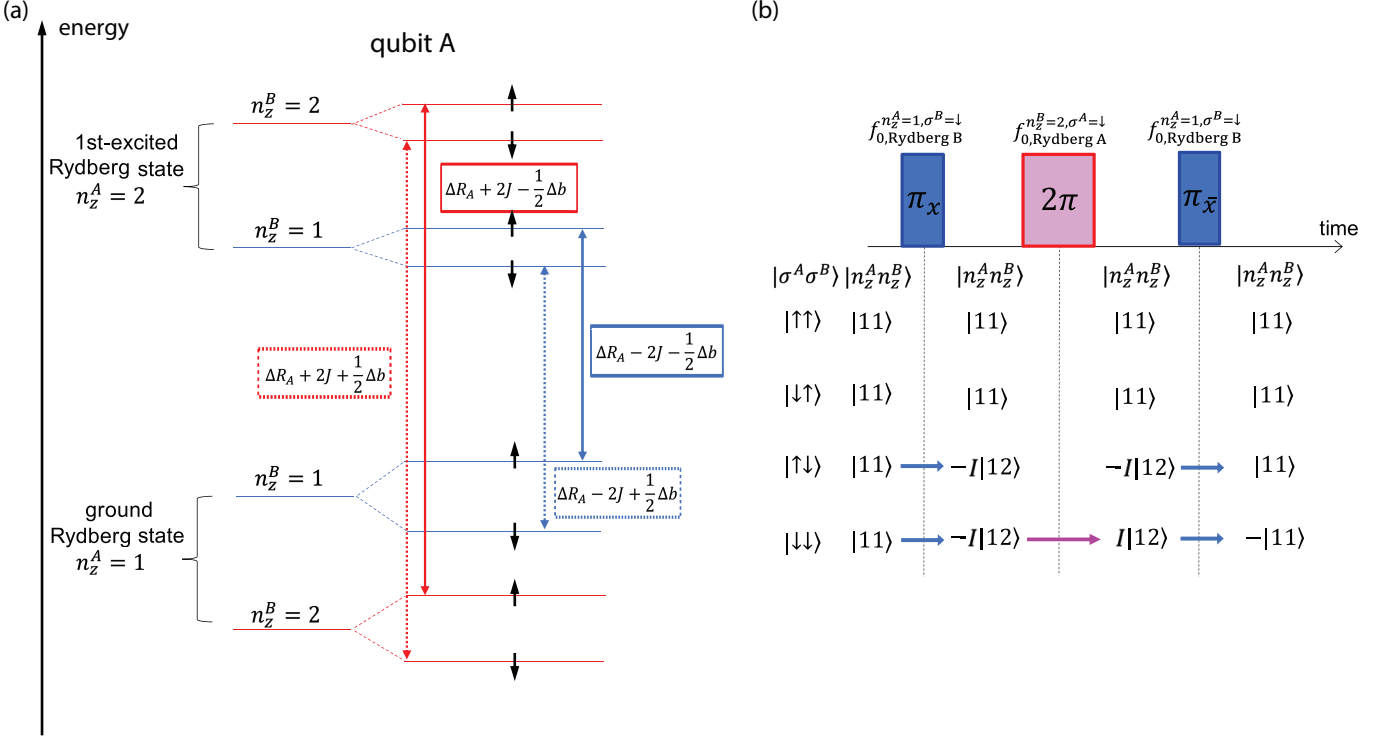


FIG. 3. (a) Energy levels of electron A for the Rydberg state of the neighboring electron $n_z^B = 1$ (shown in blue) and $n_z^B = 2$ (shown in red). The transition energy of the Rydberg state of electron A (shown with dotted arrows for $\sigma^A = -1$ and with solid arrows for $\sigma^A = 1$) depends on both the spin state of electron A and the Rydberg state of electron B. (b) MW pulse sequence to realize a controlled-phase gate. Here, we consider four possible combinations of the spin states of qubits A and B. The first and third pulses are effective only for the last two cases and the 2nd pulse is effective only for the last case. See the main text for the details.

Taking into account the first-order energy shift due to $W + W'$, the energy difference between the Rydberg-ground state and the Rydberg-1st-excited state of qubit i can be explicitly rewritten as

$$\Delta E_{n_z^i=1 \rightarrow 2} = \Delta R_i + 2J(-1)^{n_z^i} - \frac{1}{2}\Delta b \sigma^i, \quad (12)$$

where ΔR_i is the energy difference between the Rydberg-ground state and the Rydberg-1st-excited state of qubit i given by H_0 (Eq. (S5)) for a given combination of V_1 and V_2 . n_z^j is the Rydberg state of an adjacent qubit j . The transition frequency for the Rydberg state of qubit i , $f_0 = \Delta E_{n_z^i=1 \rightarrow 2}/h$, depends on the three factors: qubit i 's spin state σ^i , the Rydberg state of the adjacent qubit n_z^j , and the voltage applied to the electrodes. A MW signal is transmitted via a rectangular waveguide [41] to excite the Rydberg state (Fig. 3). Although MW is applied to all the qubits globally through the waveguide, the individual addressing of qubits is realized by tuning the Rydberg transition energy by tuning V_1 and V_2 .

Note that the electrons always stay in the Rydberg-ground state except when we perform a two-qubit gate; thus the electric dipole-dipole interaction W' does not affect the qubit states as long as both qubits A and B are in the same Rydberg state: $[W', s_j^A s_j^B] = 0$ ($j = x, y, z$). On the other hand, the magnetic dipole-dipole interaction alters the qubit states, however the evolution due to the magnetic dipole-dipole interaction is orders of magnitude slower than any quantum operation shown here [16], and thus can be neglected.

In the following, we show one way to realize a two-qubit gate, a Cirac-Zoller-type controlled-phase gate [42]. Both qubits A and B are in the Rydberg-ground state before starting the controlled-phase gate. Therefore, the initial qubit state is written as

$$a|11 \uparrow\uparrow\rangle + b|11 \downarrow\uparrow\rangle + c|11 \uparrow\downarrow\rangle + d|11 \downarrow\downarrow\rangle, \quad (13)$$

where $|n_z^A n_z^B \sigma^A \sigma^B\rangle$ is an abbreviation of $|n_z^A\rangle_A |n_z^B\rangle_B |\sigma^A\rangle_A |\sigma^B\rangle_B$ and $|a|^2 + |b|^2 + |c|^2 + |d|^2 = 1$. Fig. 3(b) presents a MW pulse sequence to realize a controlled-phase gate for qubits A and B. First, we apply a π pulse around the x axis

with MW frequency $\omega_{\text{MW}}/2\pi = f_{0, \text{RydbergB}}^{n_z^A=1, \sigma^B=\downarrow} = (\Delta R_B - 2J + \frac{1}{2}\Delta b)/h$. The Rydberg state of qubit B is excited when the Rydberg state of qubit A is the ground state ($n_z^A = 1$) and the spin state of qubit B is spin-down ($\sigma^B = -1$). Consequently, the qubit state becomes

$$a |11 \uparrow\uparrow\rangle + b |11 \downarrow\uparrow\rangle - Ic |12 \uparrow\downarrow\rangle - Id |12 \downarrow\downarrow\rangle. \quad (14)$$

Second, we apply a 2π pulse around the x axis with MW frequency $\omega_{\text{MW}}/2\pi = f_{0, \text{RydbergA}}^{n_z^B=2, \sigma^A=\downarrow} = (\Delta R_A + 2J + \frac{1}{2}\Delta b)/h$. Thus, the qubit state becomes

$$a |11 \uparrow\uparrow\rangle + b |11 \downarrow\uparrow\rangle - Ic |12 \uparrow\downarrow\rangle + Id |12 \downarrow\downarrow\rangle. \quad (15)$$

Third, we apply a π pulse around $-x$ axis with the same MW frequency as the first pulse. Consequently, the qubit state becomes

$$a |11 \uparrow\uparrow\rangle + b |11 \downarrow\uparrow\rangle + c |11 \uparrow\downarrow\rangle - d |11 \downarrow\downarrow\rangle. \quad (16)$$

Compared to the initial qubit state (Eq. (13)), the sign of the phase is changed only when the initial state of both qubits A and B is spin-down. In total, a controlled-phase gate for the spin states has been realized by the three MW pulses.

The Rydberg transition rate can be tuned by the power of the MW sent through a waveguide (Fig. 1(d)). The Hamiltonian for the electron interaction with the vertical electric field of the MW is $eE^{\text{MW}} \cos(\omega_{\text{MW}}t)z$ and the transition rate, which determines the two-qubit gate speed, is expressed as

$$f_1 = \langle n_z^i = 1, \sigma^i | eE^{\text{MW}} z | n_z^i = 2, \sigma^i \rangle / 2h = eE^{\text{MW}} z_{12} / 2h, \quad (17)$$

and can reach 50 MHz [29] with $E^{\text{MW}} = 1$ V/cm (which corresponds to about 2 μW of EM wave power through a 1 mm² rectangular waveguide) and $z_{12} = 4$ nm.

We should carefully tune the Rydberg transition energy of the qubits so that only the Rydberg transition of the target qubit in intended states is on resonance. Taking into account the Rydberg relaxation time ($1/\Gamma_1 = T_1 = T_2/2 \sim 1 \mu\text{s}$) [28, 29], the fidelity of a controlled-phase gate is calculated to be $\sim 99\%$ with $4J/h = \Delta b/h = 137$ MHz and $f_1 = 35.5$ MHz (see the supplementary information for more details). In fact, the target qubit in unintended states also acquires some phase during the Rydberg excitation through the Rydberg-spin interaction and the electric dipole-dipole interaction. We show how this effect can be compensated in the supplementary information. The proposed pulse sequence is one of the ways to realize a two-qubit gate. For example, we could also realize a controlled-phase gate by waiting time $\pi/4J$ after exciting the electrons to the 1st-excited Rydberg state. Alternatively, making use of the Rydberg-blockade or Rydberg-antiblockade effect, we may be able to realize a two-qubit gate with fewer steps or with a shorter time [43–46]. Another improvement may be achieved by using such an optimal pulse as a GRAPE pulse to avoid populating leakage levels or suppressing the phase acquired by the AC Stark shift [47]. However, those are beyond the scope of this paper.

VIII. READ-OUT OF THE QUBIT STATE

By spin-selectively exciting the Rydberg state and detecting the image-charge change induced by the Rydberg excitation using an LC circuit, a QND read-out for the spin state can be realized.

As shown in Fig. 1(b,c), the vertical position of the electron is changed by $z_{22} - z_{11} = 11.5$ nm for $V_1 = 60$ mV, and $V_2 = -45$ mV, when the Rydberg state is excited from the ground state to the 1st excited state. By applying a higher voltage to V_1 , the electron is more strongly attracted to the helium surface and the change in vertical position by excitation of the Rydberg state becomes smaller. A COMSOL simulation (see the supplementary for more details) shows that the excitation from the Rydberg-ground state to the Rydberg-1st-excited state changes the image charge induced on the center electrode by $\Delta q \sim 0.01e$ (Fig. 1(b,c)) for $V_1 = 60$ mV and $V_2 = -45$ mV. As shown earlier (Fig. 3(a)), we can spin-selectively excite the Rydberg state. For example, by setting a MW frequency to $f_{0, \text{RydbergA}}^{n_z^B=1, \sigma^A=\uparrow}$, the image charge change occurs only when qubit A is in spin-up state. Under MW excitation, the induced image charge on the center electrode is $\Delta Q = \rho_{22}\Delta q$, where ρ_{22} is the probability of the electron to occupy the Rydberg-1st-excited state of qubit A, which depends on the MW frequency detuning from the resonance: $\Delta\omega_0 = \omega_{\text{MW}} - 2\pi f_{0, \text{RydbergA}}^{n_z^B=1, \sigma^A=\uparrow}$ (Fig. 3(a)). Furthermore, we apply a small and slow voltage modulation (probe signal) $u_m \cos(\omega_m t)$ to the center electrode. The detuning from the resonance is modulated due to the Stark shift of the Rydberg energy levels and the time-averaged induced image charge on the center electrode can be approximated by

$\Delta Q = \overline{\rho_{22}}(t)\Delta q$. Here, $\bar{\cdot}$ denotes the average over time much longer than $2\pi/\omega_{\text{MW}}$ but much shorter than $2\pi/\omega_m$. Therefore, the charge on the center electrode is expressed as $Q = C_0 u_m \cos(\omega_m t) + \Delta Q$ where C_0 is the stray capacitance of the center electrode. The stray capacitance of such a nano-fabricated device is dominated by the bond pads and is typically ~ 1 pF [37]. Focusing on the in-phase component of ΔQ in response to the voltage modulation, the charge on the center electrode is rewritten as $Q \approx (C_0 + \Delta C)u_m \cos(\omega_m t)$ with the effective capacitance change:

$$\Delta C \approx \frac{\langle \rho_{22} \rangle_I \Delta q}{u_m}, \quad (18)$$

where $\langle \rho_{22} \rangle_I = \int_{-t_c}^{t_c} \rho_{22}(t) \cos(\omega_m t) dt / t_c$ is the in-phase component of $\rho_{22}(t)$ and $t_c \gg 2\pi/\omega_m$. This effective capacitance change happens only when qubit A is in the spin-up state. By focusing on the two-lowest Rydberg states and the spin-up state, which are the states involved in this excitation, we can write the Hamiltonian of qubit A under MW excitation with the voltage modulation as

$$H' = \Delta E_{n_z^i=1 \rightarrow 2} s_z^A + eE^{\text{MW}} z \cos(\omega_{\text{MW}} t) + eE^m z \cos(\omega_m t), \quad (19)$$

where s_z^A was defined earlier. In the rotating reference frame of the angular frequency ω_{MW} , H' (Eq. (19)) can be approximated by

$$H_R = \Delta\omega(t)s_z^A + \Omega_1 s_x^A, \quad (20)$$

where $\Delta\omega(t) = \Delta\omega_0 + 2\pi A_m \cos(\omega_m t)$, $\Omega_1 = \frac{eE^{\text{MW}} z_{12}}{2\hbar} = 2\pi f_1$ and $2\pi A_m = eE^m(z_{22} - z_{11})/\hbar$. The time-dependent eigenstates of H_R (Eq. (20)) can be expressed with a density operator $\rho(t) = \sum_{(\eta,\zeta)=(1,2)} \rho_{\eta\zeta}(t) |n_z^i = \eta\rangle \langle n_z^i = \zeta|$. The solution to the equation of motion with the Hamiltonian H_R (Eq. (20)) is known as exhibiting a sequence of Landau-Zener transitions [48–50]. We numerically calculated the time-dependent eigenstates of H_R and obtained $\rho_{22}(t)$ numerically (see supplementary for more details). The calculation results are shown as $\langle \rho_{22} \rangle_I$ in Fig. 4 (c-e).

In order to estimate the effective capacitance change, we calculate the lever arm of the voltage applied to the center electrode to the Rydberg transition energy shift $\alpha' = 2$ GHz/mV (see the supplementary information for more details). The effective capacitance change can be rewritten as $\Delta C = \alpha' \Delta q \frac{\langle \rho_{22} \rangle_I}{A_m}$. $\frac{\langle \rho_{22} \rangle_I}{A_m}$ is maximized around black circle positions in Fig. 4 (e), where $\langle \rho_{22} \rangle_I \approx 0.1$ and $A_m = f_1/10 = 5$ MHz, which gives $\Delta C \approx 60$ aF. The effective capacitance change can be detected as the change in the resonance frequency of the LC resonant circuit. The LC resonant circuit is formed by connecting an inductance to the center electrode as done in semiconductor quantum dots [37, 51]. Recently the capacitance sensitivity was measured to be as high as 0.04 aF/ $\sqrt{\text{Hz}}$ [52]. This allows us to detect $\Delta C \approx 60$ aF at the signal-to-noise ratio ≈ 1 with the measurement bandwidth ~ 1 MHz, with which we can expect to have a fast enough qubit-state read-out for topological quantum error correction [1]. Summarizing the above, we can read out the qubit state (the spin state) by detecting the Rydberg transition via the measurement of the LC resonance frequency. This read-out technique works as a QND measurement [53] for the spin state. A QND is obtained if the Hamiltonian of the system including a measurement apparatus commutes with an observable. In our case, the observable is the z projection of the spin state of qubit i , while the measurement apparatus is the Rydberg state of qubit i . The Hamiltonian of qubit i is given by

$$H^i = \frac{1}{2} \Delta R_i s_z^i + \sum_j J s_z^i s_z^j + \frac{1}{2} g \mu_B B \sigma_z^i - \frac{1}{2} \Delta b \sigma_z^i s_z^i, \quad (21)$$

where \sum_j is the sum over the nearest neighbor qubits of qubit i . From Eq. (21), we obtain $[\sigma_z^i, H^i] = 0$.

$\sum_j J s_z^i s_z^j$ in Eq. (21) tells us that we cannot realize the two-qubit gate or the read-out of the qubit state for the nearest neighbor qubits at the same time. If one or more nearest neighbors of an electron are in the Rydberg-excited state, then also exciting this electron will result in the electrons' states being altered unintentionally. Although this fact sets some constraints on how to realize quantum gates, we expect only a minor impact since the read-out of the qubit state and the two-qubit gate can be performed much faster than the spin coherence time.

IX. SUMMARY AND DISCUSSIONS

In summary, we propose a hybrid qubit system consisting of the Rydberg states and the spin states of electrons on the surface of liquid helium. An artificially-introduced magnetic field gradient induces the spin-orbit interaction and the Rydberg-spin interaction, which allows us to coherently control the spin state electrically and perform a two-qubit

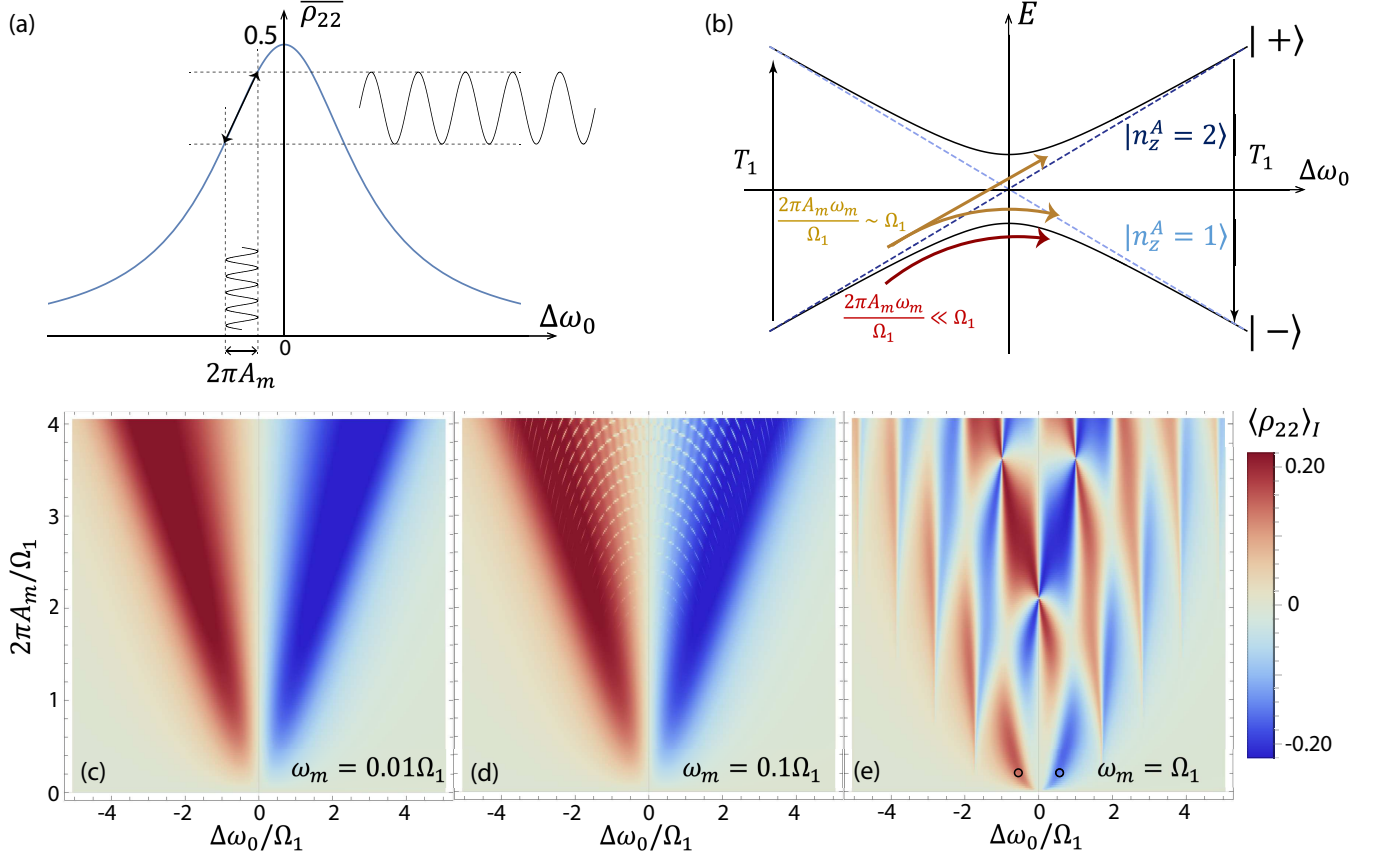


FIG. 4. (a) Time-averaged probability of the electron in the excited state $\overline{\rho_{22}}$ as a function of the detuning of excitation frequency. $\overline{\rho_{22}}$ reaches its maximum value at $\Delta\omega_0 = 0$. Under the condition that the Rydberg transition rate is much faster than the Rydberg relaxation: $\Omega_1 \gg 1/T_1, 1/T_2$, the maximum value is ~ 0.5 . (b) Energy levels E versus the MW frequency detuning $\Delta\omega_0$. The detuning is modulated with an amplitude of $2\pi A_m$ and a frequency of $f_m = \omega_m/2\pi$. $|\pm\rangle$ are the eigenstates of H_R (Eq. (20)) without voltage modulation ($A_m = 0$) and $|n_z^A = 1\rangle$ and $|n_z^A = 2\rangle$ are those without MW excitation ($\Omega_1 = 0$). The state-relaxation happens from $|n_z^A = 2\rangle$ and $|n_z^A = 1\rangle$ (see the supplementary information for more details). When $2\pi A_m \omega_m / \Omega_1 \gg \Omega_1$, the LZ transition reaches the fast-passage limit and the electron always stays in $|n_z^A = 0\rangle$ (that is, ρ_{22} always stays 0) after time T_1 . When $2\pi A_m \omega_m / \Omega_1 \sim \Omega_1$, the state is changed from $|+\rangle$ to $|-\rangle$ or vice versa with some probability p and stays in the same state with the probability of $1 - p$, which results in LZ interference patterns shown in (d,e). When $2\pi A_m \omega_m / \Omega_1 \ll \Omega_1$, the LZ transition reaches the slow-passage limit and the state always stays in $|-\rangle$. (c-e) Numerically calculated in-phase component of the fraction in the excited state $\langle \rho_{22} \rangle_I$ as a function of normalized detuning $\Delta\omega_0/\Omega_1$ and the modulation amplitude $2\pi A_m/\Omega_1$ for the modulation frequency $\omega_m = 0.01\Omega_1$, $\omega_m = 0.1\Omega_1$, and $\omega_m = \Omega_1$ in (c), (d), and (e), respectively. The relation between the Rydberg relaxation rate and the Rydberg transition rate is set as $\frac{1}{T_1} = \frac{2}{T_2} = \frac{\Omega_1}{2\pi \cdot 50}$.

gate for the spin state via the Coulomb interaction. The electrons are trapped on top of pillars, separated by a distance of $0.88 \mu\text{m}$, which allows the electric dipole-dipole interaction between the electrons to be as strong as $\approx 140 \text{ MHz}$. The introduced magnetic field gradient mixes the spin state and the orbital state and shortens the spin relaxation time to 50 ms for the configurations that we considered here. At the same time, the existence of the magnetic field gradient does not degrade the spin dephasing time and it stays around 100 s at liquid helium temperature $\sim 100 \text{ mK}$. The Rabi frequency for the spin rotation is more than 10^6 times higher than the spin relaxation and we estimated the single-qubit gate fidelity to be $> 99.9999\%$. However, we suspect that in real experiments it must be limited by other experimental sources such as the phase noise of the MW generator [54]. As a two-qubit gate is realized by the coherent control of the Rydberg transition, its fidelity is limited by the Rydberg relaxation rate. With the Rydberg relaxation rate $\Gamma_1 \sim 1 \text{ MHz}$, the fidelity of a controlled-phase gate was estimated to be $\sim 99\%$. Further improvements in the two-qubit gate scheme are expected. The quantum-non-demolition measurement of the qubit state is achieved via the Rydberg-spin interaction by detecting the Rydberg transition of the qubit using a resonant LC-circuit with a measurement bandwidth $\sim 1 \text{ MHz}$.

We believe that the experimental demonstration for a few number of qubits can be readily done since the proposed

device geometry is similar to the devices with which trapping a single electron on helium was achieved [9, 18, 20, 55] and we can make use of the well-established fabrication technique of a nano-scale ferromagnet for semiconductor quantum dots [35, 56, 57]. Together with its feasibility of employing the three-dimensional wiring techniques under development [26, 58, 59], this architecture makes electrons on helium a strong candidate to realize a fault-tolerant quantum computer.

ACKNOWLEDGEMENT

We acknowledge Yury Mukharsky and John Morton, Yuichi Nagayama, Asher Jennings, and Atsushi Noguchi for useful discussions.

This work was supported by JST-FOREST, RIKEN-Hakubi program, and “KICKS” grant from Okinawa Institute of Science and Technology (OIST) Graduate University.

S.I. ELECTRON WAVEFUNCTION

In this work, we consider the case where the helium depth is 140 nm, which is thinner than the case considered in Ref. [15], where the helium depth is 500 nm. In addition to this difference, here, we have segmented toroidal electrodes (outer electrodes). We need to use a thin helium film in order to obtain a large enough magnetic field gradient at the position of the electron. Additionally, the center electrode should be close enough to the electron to obtain a large enough image charge difference between the Rydberg ground state and the Rydberg first excited state.

The electric potential felt by the electron $V(x, y, z)$ can be divided into three parts, that is $V(x, y, z) = V_{\text{ImageHe}} + V_{\text{ImageElectrodes}} + V_{\text{VoltageElectrodes}}$, where V_{ImageHe} is the potential created by the electrostatic image of the electron in liquid helium, $V_{\text{ImageElectrodes}}$ is the potential created by the electrostatic image in the electrodes, and $V_{\text{VoltageElectrodes}}$ is the potential created by the voltage applied to the electrodes. The helium depth 140 nm is high enough to neglect the image charge induced on the electrodes by the image charge in helium. Thus, we can treat the image charge in liquid helium and the image charge on the electrodes separately. The potential created by the electrostatic image in liquid helium is written as $V_{\text{ImageHe}} = \frac{\epsilon_{\text{He}} - 1}{\epsilon_{\text{He}} + 1} \frac{e}{16\pi\epsilon_0 z}$, where ϵ_0 is the electrical permittivity of vacuum and ϵ_{He} is the relative permittivity of liquid helium-4. Differently from the case treated in Ref. [15], here, the helium depth 140 nm is so small that $V_{\text{ImageElectrodes}}$ and $V_{\text{VoltageElectrodes}}$ cannot be written as a simple analytical expression or cannot be separated into the z direction and the x, y direction components. Instead, they were obtained numerically by solving the Poisson's equation by the finite element method using COMSOL. For calculating $V_{\text{ImageElectrodes}}$, we approximate an electron by a small spherical conductor whose surface charge is equal to the elementary charge and which is placed at an arbitrary position. In order to eliminate the contribution to the electron energy from the electric potential due to the electron itself, we subtract the calculated potential without electrodes from the calculated potential with all electrodes included. To calculate $V_{\text{VoltageElectrodes}}$, we separately calculate the potential due to each electrode by applying 1 V on a single electrode, while keeping all the other electrodes grounded and sum them together.

Now we consider the case where a static magnetic field $\mathbf{B} = B\mathbf{e}_z$ is applied normal to the helium surface and thus the electron is trapped both magnetically and electrically. Using the symmetric gauge: $\mathbf{A} = \frac{B\mathbf{e}_z \times \mathbf{r}}{2} = \left(-\frac{By}{2}, \frac{Bx}{2}, 0\right)$, the stationary Schrödinger equation with such a magnetic field can be written as

$$H\Phi(x, y, z) = E\Phi(x, y, z) \quad (\text{S1})$$

with

$$H = \frac{(p_x - \frac{eB}{2}y)^2}{2m_e} + \frac{(p_y + \frac{eB}{2}x)^2}{2m_e} - eV(x, y, z) \quad (\text{S2})$$

$$= \frac{p_x^2}{2m_e} + \frac{p_y^2}{2m_e} + \frac{1}{2}\omega_c L_z + \frac{1}{8}m_e\omega_c^2 r^2 - eV(x, y, z), \quad (\text{S3})$$

where $\omega_c = eB/m_e$ is the cyclotron frequency, $L_z = p_y x - p_x y$ and $r = \sqrt{x^2 + y^2}$ (see Fig. 1(a) of the main text).

In calculations presented here, we assume the same DC voltage applied to the two outer electrodes. The gap between the outer electrodes is sufficiently small compared to the liquid helium depth and ergo the DC electric potential is approximately azimuthally symmetric. Therefore, the two outer electrodes can be approximated by a hollow cylinder of outer diameter 900 nm and of inner diameter 300 nm (Fig. 1(a) of the main text). The electric potential and the wavefunction can be written as $V(r, z)$ and $\Phi(r, z, \theta) = \phi_{m, n_r, n_z}(r, z)\psi_m(\theta)$, respectively, which satisfy

$$H\phi_{m, n_r, n_z}(r, z) = E_{m, n_r, n_z}^{(0)}\phi_{m, n_r, n_z}(r, z), \quad (\text{S4})$$

with

$$H = -\frac{\hbar^2}{2m_e} \left(\frac{1}{r} \frac{\partial}{\partial r} + \frac{\partial^2}{\partial r^2} + \frac{\partial^2}{\partial z^2} - \frac{m^2}{r^2} \right) + \frac{1}{2}\hbar\omega_c m + \frac{1}{8}m_e\omega_c^2 r^2 - eV(r, z), \quad (\text{S5})$$

and

$$\frac{\partial^2}{\partial \theta^2} \psi_m(\theta) = -m^2 \psi_m(\theta), \quad (\text{S6})$$

where the (r, θ) plane is parallel to the liquid surface and $m = 0, \pm 1, \pm 2, \pm 3 \dots$

We solved Eq. (S4) numerically with the electric potential $V(r, z)$ calculated as described earlier. Even though $V(r, z)$ cannot be separated into the in-plane (r) and the vertical (z) components, we can still label the eigenfunctions $\phi_{m, n_r, n_z}(r, z)$ by the quantum numbers n_r and n_z associated with the electron's in-plane orbital motion (orbital state)

and vertical orbital motion (Rydberg state), respectively, with $n_r = 0, 1, 2, 3\dots$ and $n_z = 1, 2, 3\dots$. Fig. S1(a–c) show the normalized eigenfunctions for $(m, n_r, n_z) = (0, 0, 1)$ and $(m, n_r, n_z) = (0, 0, 2)$ for $V_1 = V_2 = 0$ and $B = 0$, and the corresponding eigenenergies as a function of the cyclotron frequency determined by the applied magnetic field B , respectively. Fig. S1(d–f) show the same information for the case $V_1 = 60$ mV and $V_2 = -45$ mV.

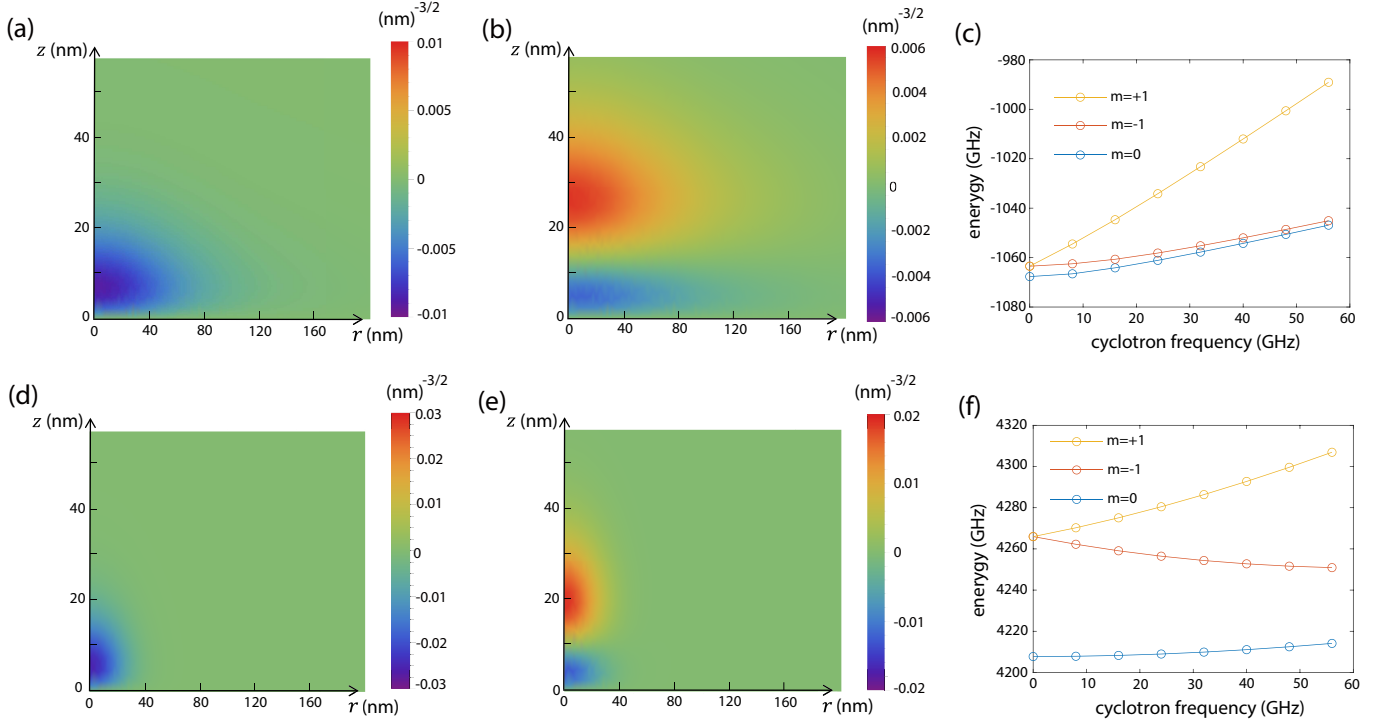


FIG. S1. Normalized eigenfunction $\phi(r, z)$ for $(m, n_r, n_z) = (0, 0, 1)$ in (a) and $= (0, 0, 2)$ in (b) with $V_1 = V_2 = 0$ and $B = 0$ and $(m, n_r, n_z) = (0, 0, 1)$ in (d) and $= (0, 1, 2)$ in (e) with $V_1 = 60$ mV, $V_2 = -45$ mV and $B = 0$. (c) The energy eigen values for $m = 0, \pm 1$ and $(n_r, n_z) = (0, 1)$ as a function of the cyclotron frequency $\omega_c = eB/m_e$ with $V_1 = V_2 = 0$. (f) The same as in (c) with $V_1 = 60$ mV, $V_2 = -45$ mV.

Fig. S2(a) shows how the Rydberg and orbital transition energies change as a function of V_1 , when V_2 is set to 0. With increasing V_1 , both the orbital and the Rydberg transition energies increase. Fig. S2(c) and (d) shows the average vertical position of the electron wavefunction as a function of V_1 and V_2 , respectively. The electron is confined more tightly by increasing V_1 and V_2 and comes closer to the liquid surface. Fig. S2(b) shows the transition energies as a function of V_2 for $V_1 = 60$ mV and 100 mV. In this case, the Rydberg transition energy decreases as V_2 decreases, while the orbital transition energy increases. As shown in Sec. S.II B, with higher orbital transition energies, one can suppress the relaxation rate and the dephasing rate of the spin state (see Fig. S4 and Fig. S5). At the same time, unfortunately, the Rabi frequency of the spin state is also suppressed (Fig. S3).

S.II. SINGLE-QUBIT GATES

A. Coherent control of the spin state

The Hamiltonian of the interaction of an electron with a classical AC electric field with an amplitude E^{EDSR} and polarization along the x axis is given by $V^{\text{EDSR}}(t) = Ue^{-i\omega_{\text{EDSR}}t} + U^\dagger e^{i\omega_{\text{EDSR}}t}$ with $U = eE^{\text{EDSR}}x/2$. The total Hamiltonian which is responsible for the coherent control of the spin state can be described as

$$H(t) = V^{\text{EDSR}}(t) + W_r, \quad (\text{S7})$$

where W_r is given by Eq. (4) of the main text. The spin-flip transition happens due to the second-order process and the transition rate can be written as

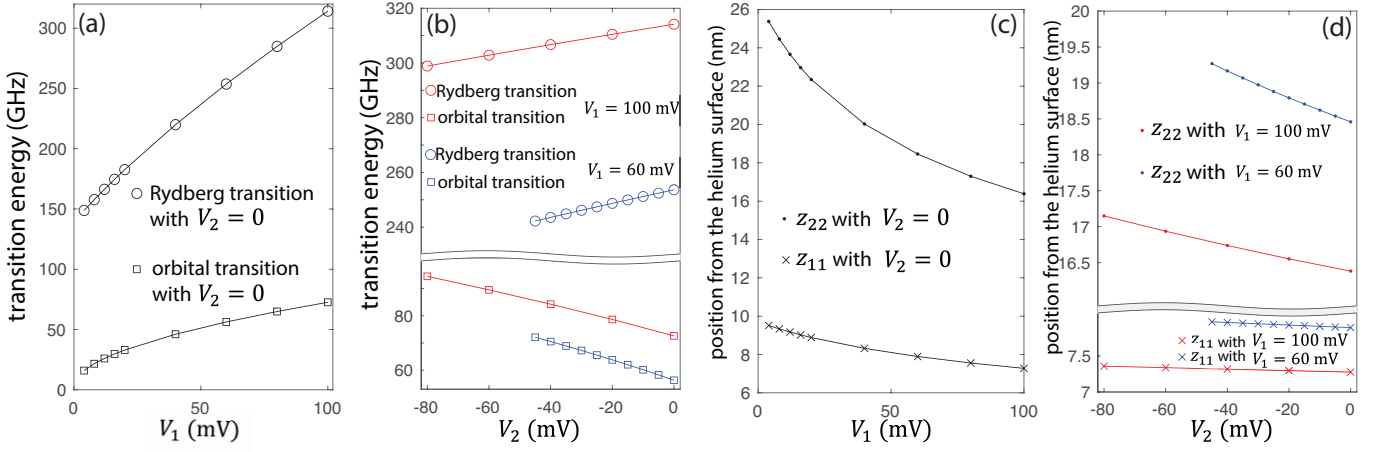


FIG. S2. The magnetic field is set to 0 in (a-d). (a) Transition energies as a function of V_1 with $V_2 = 0$. Circles represent the transition energy between the two lowest Rydberg states, $E_{(m,n_r,n_z)=(0,0,2)}^{(0)} - E_{(m,n_r,n_z)=(0,0,1)}^{(0)}$. Squares represent the transition energy between the two lowest in-plane orbital states, $E_{(m,n_r,n_z)=(0,1,1)}^{(0)} - E_{(m,n_r,n_z)=(0,0,1)}^{(0)}$. (b) Red and blue circles represent the transition energies between the two lowest Rydberg states as a function of V_2 with $V_1 = 100$ mV and with $V_2 = 60$ mV, respectively. Red and blue squares represent the transition energies between the two lowest orbital states as a function of V_2 with $V_1 = 100$ mV and with $V_2 = 60$ mV, respectively. (c) The dots represent the average position of the Rydberg-1st-excited state along the z axis and the crosses represent that of the Rydberg-ground state as a function of V_1 with $V_2 = 0$. (d) The red and blue dots represent the average position of the Rydberg-1st-excited state along the z axis as a function of V_2 with $V_1 = 100$ mV and $= 60$ mV, respectively. The red and blue crosses represent the average position of the Rydberg-ground state along the z axis as a function of V_2 with $V_1 = 100$ mV and $= 60$ mV, respectively.

$$\Gamma_{\text{EDSR}} = \frac{d}{dt} \left(\lim_{t \rightarrow \infty} \frac{-1}{\hbar^2} \int_0^t dt' \int_0^{t'} dt'' \langle f | H(t') H(t'') | i \rangle \right)^2 \approx \frac{2\pi}{\hbar} \left| \frac{(W_r)_{f\beta}(U)_{\beta i}}{E_i - E_\beta + \hbar\omega_{\text{EDSR}}} + \frac{(U)_{f\beta'}(W_r)_{\beta' i}}{E_i - E_{\beta'}} \right|^2 \delta(E_f - E_i - \hbar\omega_{\text{EDSR}}), \quad (\text{S8})$$

where $i = (m = 0, \downarrow)$, $f = (m = 0, \uparrow)$, $\beta = (m = +1, \downarrow)$, and $\beta' = (m = -1, \uparrow)$. $(W_r)_{\Delta, \circ}$ and $(U)_{\Delta, \circ}$ stand for the matrix elements $\langle \circ | W_r | \Delta \rangle$ and $\langle \circ | U | \Delta \rangle$, respectively. Here we take into account only the virtual transitions from $m = 0$ to $m = \pm 1$ states with $n_r = 0$ and $n_z = 1$. The contribution from the higher intermediate states is much smaller and thus is ignored. The first (second) term of the last expression corresponds to the transition process shown with red (light blue) arrows in Fig. 2(d) of the maintext. From Eq. (S8), we obtain the Rabi frequency

$$f_{\text{Rabi}} = \frac{1}{2\pi\hbar} \left| \frac{(W_r)_{f\beta}(U)_{\beta i}}{E_i - E_\beta + \hbar\omega_{\text{EDSR}}} + \frac{(U)_{f\beta'}(W_r)_{\beta' i}}{E_i - E_{\beta'}} \right| = \frac{1}{8} \partial_r f_{b_r} \partial_x f_{\text{AC}} l_0^2 \left| \frac{1}{f_i - f_\beta + f_{\text{EDSR}}} + \frac{1}{f_i - f_{\beta'}} \right|, \quad (\text{S9})$$

where $l_0 = |\langle \phi_{m=0, n_r=0, n_z=1} | r | \phi_{m=\pm 1, n_r=0, n_z=1} \rangle|$, $\partial_r f_{b_r} = g\mu_B \frac{db_r}{dr} / \hbar$, $\partial_x f_{\text{AC}} = eE^{\text{EDSR}} / \hbar$, $f_\square = E_\square / \hbar$ for $\square = i, \beta, \beta'$ and $f_{\text{EDSR}} = \omega_{\text{EDSR}} / 2\pi$. Our numerical simulation shows that the cobalt pillar creates a magnetic field gradient $\frac{db_r}{dr} = 0.23$ mT/nm at the position of the electron in the magnetic field applied along the z axis, when the cobalt pillar is fully magnetized and it reaches the saturation magnetization (1.8 T). Fig. S3 shows the numerically calculated Rabi frequency for various V_1 and V_2 , assuming $\omega_c \approx \omega_{\text{EDSR}} = 16$ GHz and $E^{\text{EDSR}} = 500$ V/cm. We simulated the Rabi frequency for the magnetic field B in the range of 0 to 2 T and found that the Rabi frequency varies with the magnetic field by less than 20 % except for the case when the applied voltages are $V_1 = V_2 = 0$ (Fig. S3).

B. Longitudinal relaxation of the spin state

As the spin-flip transition described in Sec. S.II A, the spin relaxation also happens due to the second-order process. The in-plane magnetic field gradient, whose Hamiltonian is W_r , is responsible for the simultaneous flipping of the orbital state and the spin state, while the orbital transition is due to the two-ripplon scattering, whose Hamiltonian is H_{2r_i} . The spin relaxation is an energy non-conserving process and it was previously demonstrated that a process

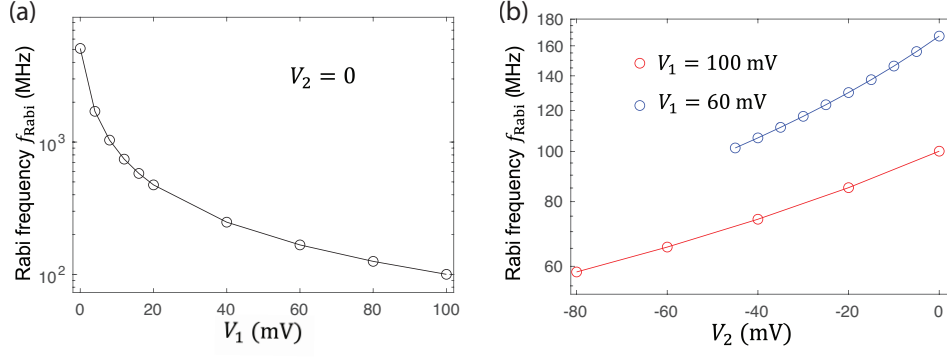


FIG. S3. Rabi frequency of the spin state as a function of V_1 with $V_2 = 0$ in (a) and as a function of V_2 with $V_1 = 100$ mV (red circles) and with $V_1 = 60$ mV (blue circles) in (b) when the cyclotron frequency of the electron corresponds to $\omega_c = eB/m_e = 16$ GHz.

that requires an energy change of $\gg k_B T$ is dominated by the two-rippion emission of short wavelength capillary waves [40]. Here, k_B is the Boltzmann constant and T is the liquid helium temperature. Accordingly, the Hamiltonian corresponding to the two-rippion emission is written as [40]

$$H_{2ri}^F = \frac{1}{2} \sum_{\mathbf{q}_1} \sum_{\mathbf{q}_2} Q_{\mathbf{q}_1} Q_{\mathbf{q}_2} \hat{F} e^{i(\mathbf{q}_1 + \mathbf{q}_2) \cdot \mathbf{r}} a_{-\mathbf{q}_1}^\dagger a_{-\mathbf{q}_2}^\dagger, \quad (\text{S10})$$

where $\langle \mathbf{n} | \hat{F} | \mathbf{n}' \rangle = F_{\mathbf{n}\mathbf{n}'} = 2\kappa_0 \sqrt{\left(\frac{\partial v}{\partial z}\right)_{\mathbf{n}\mathbf{n}} \left(\frac{\partial v}{\partial z}\right)_{\mathbf{n}'\mathbf{n}'}}$, $\kappa_0 = \sqrt{2m_e V_0}/\hbar$, $V_0 \approx 1$ eV is the barrier at the helium surface and v is the energy of the electron in the electric potential created by the image charge and externally applied electric field. Rippions are emitted to transfer the energy lost by the electron to the ripplon systems. In order to satisfy the conservation of the total momentum of an electron and rippions, two rippions must be emitted in nearly opposite directions, that is $\mathbf{q}_1 \sim -\mathbf{q}_2$. The total Hamiltonian which is responsible for the relaxation of the spin state can be written as

$$H = H_{2ri}^F + W_r. \quad (\text{S11})$$

According to the Fermi's golden rule in the second order of the perturbation theory,

$$\Gamma_{\text{relaxation}} \approx \frac{2\pi}{\hbar} \left| \frac{(W_r)_{f\beta'} (H_{2ri}^F)_{\beta'i}}{E_i - E_{\beta'} + \epsilon_{n_{ri}} - \epsilon_{n'_{ri}}} + \frac{(H_{2ri}^F)_{f\beta} (W_r)_{\beta i}}{E_i - E_\beta} \right|^2 \delta(E_f - E_i + \epsilon_{n'_{ri}} - \epsilon_{n_{ri}}), \quad (\text{S12})$$

where n_{ri} and n'_{ri} collectively stand for the states of all the rippions before and after the two-rippion emission, respectively, and therefore $\epsilon_{n'_{ri}} - \epsilon_{n_{ri}} = 2\hbar\omega_q$, where $\hbar\omega_q \equiv \hbar\omega_{\mathbf{q}_1} \sim \hbar\omega_{\mathbf{q}_2}$ is the energy of the emitted ripplon. $(H_{2ri}^F)_{\Delta, \circ}$ stands for $\langle \circ, n_{ri} | H_{2ri}^F | \Delta, n'_{ri} \rangle$. The definition of the states i , f , β and β' is the same as in Sec. S.II A: $i = (m = 0, \downarrow)$, $f = (m = 0, \uparrow)$, $\beta = (m = +1, \downarrow)$, and $\beta' = (m = -1, \uparrow)$. As done in the previous section, we take into account only the $n_r = 0$, $n_z = 1$, and $m = 0, \pm 1$ states. Using the explicit form: $(W_r)_{f\beta'} = (W_r)_{\beta i} = \frac{\hbar}{2} \partial_r f_{b_r} l_0$ and the relation $(H_{2ri}^F)_{\beta'i} = (H_{2ri}^F)_{f\beta}$, Eq. (S12) is further reduced to $\Gamma_{\text{relaxation}} \approx \frac{2\pi}{\hbar} |(H_{2ri}^F)_{f\beta}|^2 \frac{1}{4} (\partial_r f_{b_r})^2 l_0^2 \left| \frac{1}{f_i - f_\beta + f_{\text{EDSR}}} + \frac{1}{f_i - f_{\beta'}} \right|^2 \delta(E_f - E_i + \epsilon_{n'_{ri}} - \epsilon_{n_{ri}})$. Using the explicit form of H_{2ri}^F , we obtain

$$\begin{aligned} & |(H_{2ri}^F)_{f\beta}|^2 \delta(E_f - E_i + \epsilon_{n'_{ri}} - \epsilon_{n_{ri}}) \\ & \approx 2 \sum_{\mathbf{q}} \sum_{\mathbf{s}} Q_{\mathbf{q}}^4 \kappa_0^2 \sum_k i^k |\langle \psi_{m=0}(\theta) | e^{Ik\theta} | \psi_{m=\pm 1}(\theta) \rangle \langle \phi_{m=0, n_r=0, n_z=1} | \frac{\partial v}{\partial z} J_k(sr) | \phi_{m=\pm 1, n_r=0, n_z=1} \rangle|^2 \delta(\hbar\omega_{\text{EDSR}} - 2\hbar\omega_q), \end{aligned} \quad (\text{S13})$$

where $s = |\mathbf{q}_1 + \mathbf{q}_2|$ and J_1 is the Bessel function of the 1st kind. By inserting the identity operator $\mathbf{I} = \sum_{n_r, n_z} |\phi_{m=0, n_r, n_z}\rangle \langle \phi_{m=0, n_r, n_z}|, \langle \phi_{m=0, n_r=0, n_z=1}| \frac{\partial v}{\partial z} J_1(sr) | \phi_{m=\pm 1, n_r=0, n_z=1}\rangle$ can be approximated by

$\langle \phi_{m=0, n_r=0, n_z=1} | \frac{\partial v}{\partial z} | \phi_{m=0, n_r=0, n_z=1} \rangle \langle \phi_{m=0, n_r=0, n_z=1} | J_1(sr) | \phi_{m=\pm 1, n_r=0, n_z=1} \rangle$. We numerically confirmed that the other terms are negligibly small. This results in

$$\Gamma_{\text{relaxation}} \approx \frac{m_e V_0 (\partial_r f_{b_r})^2 l_0^2}{12 \hbar \rho_{\text{He}}^{2/3} \alpha_{\text{He}}^{4/3} \omega_{q^*}^{1/3}} \left| \langle \phi_{m=0, n_r=0, n_z=1} | \frac{\partial v}{\partial z} | \phi_{m=0, n_r=0, n_z=1} \rangle \right|^2 \times \int s \left| \langle \phi_{m=0, n_r=0, n_z=1} | J_1(sr) | \phi_{m=\pm 1, n_r=0, n_z=1} \rangle \right|^2 ds \left| \frac{1}{f_i - f_{\beta'} - f_{\text{EDSR}}} + \frac{1}{f_i - f_{\beta}} \right|^2, \quad (\text{S14})$$

where $\omega_{q^*} = \omega_{\text{EDSR}}/2 \approx \omega_c/2$. The density and the surface tension of liquid helium 4 are $\rho_{\text{He}} = 0.145 \text{ g/cm}$ and $\alpha_{\text{He}} = 0.378 \text{ erg/cm}^2$, respectively. For the Fock-Darwin model, where the magnetic field is applied along z and the $x-y$ confinement is described by a harmonic potential, we have the relation $\int s \left| \langle \phi_{m=0, n_r=0, n_z=1} | J_1(sr) | \phi_{m=\pm 1, n_r=0, n_z=1} \rangle \right|^2 ds = 1/2l_0^2$ [60]. Although we cannot naively assume that the $x-y$ confinement can be approximated by a harmonic potential, we confirmed that the above relation is approximately valid by numerical simulation for all the configurations of the voltages and the magnetic fields shown in Fig. S4. Hence, the spin relaxation rate is further simplified as

$$\Gamma_{\text{relaxation}} \approx \frac{m_e V_0 (\partial_r f_{b_r})^2}{24 \hbar \rho_{\text{He}}^{2/3} \alpha_{\text{He}}^{4/3} \omega_{q^*}^{1/3}} \left| \langle \phi_{m=0, n_r=0, n_z=1} | \frac{\partial v}{\partial z} | \phi_{m=0, n_r=0, n_z=1} \rangle \right|^2 \left| \frac{1}{f_i - f_{\beta'} - f_{\text{EDSR}}} + \frac{1}{f_i - f_{\beta}} \right|^2. \quad (\text{S15})$$

Our numerical simulation shows that $\frac{\partial b_r}{\partial r} = 0.23 \text{ mT/nm}$ at the position of the electron. Using this value, the

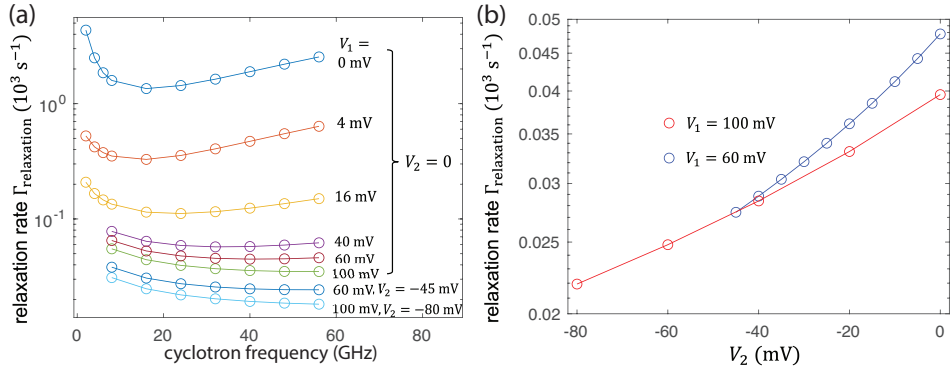


FIG. S4. Relaxation rate of the spin state as a function of ω_c for different V_1 and V_2 in (a) and as a function of V_2 with $V_1 = 100 \text{ mV}$ (red circles), with $V_1 = 60 \text{ mV}$ (blue circles) and $\omega_c = 16 \text{ GHz}$ in (b).

relaxation rate is calculated as shown in Fig. S4. Overall, the relaxation rate becomes smaller as the electric orbital confinement gets stronger (see Fig. S4). When $V_1 = 100 \text{ mV}$ and $V_2 = -80 \text{ mV}$, the relaxation time becomes as long as 100 ms. The magnetic field dependence shows the trade-off between the $\omega_q^{*-1/3}$ term and the $\left| \frac{1}{f_i - f_{\beta'} - f_{\text{EDSR}}} + \frac{1}{f_i - f_{\beta}} \right|$ term. The $\omega_q^{*-1/3}$ term becomes smaller, while the $\left| \frac{1}{f_i - f_{\beta'} - f_{\text{EDSR}}} + \frac{1}{f_i - f_{\beta}} \right|$ term becomes larger, as the magnetic field is increased.

C. Dephasing of the spin state

The spin dephasing happens due to the time fluctuation of the Zeeman energy:

$$\delta E(t) = \delta E_{\uparrow}(t) - \delta E_{\downarrow}(t), \quad (\text{S16})$$

where $\delta E_{\sigma}(t) = E_{\sigma}(t) - \overline{E_{\sigma}(t)}$, $E_{\sigma}(t)$ is the energy level at a time t and $\overline{E_{\sigma}(t)}$ is the time-averaged energy level of the spin state σ with $\sigma = \uparrow$ or \downarrow and here we consider $m = 0, n_z = 1, n_r = 0$. The phase difference between the spin-up and the spin-down states evolves over time as $\varphi(t) - \varphi(0) = \frac{1}{\hbar} \int_0^t \delta E(t') dt'$. The ensemble average of the phase evolution is given by

$$\langle [\varphi(t) - \varphi(0)]^2 \rangle = \frac{1}{\hbar^2} \int_0^t dt' \int_0^t dt'' \langle \delta E(t') \delta E(t'') \rangle. \quad (\text{S17})$$

We assume that the successive samples of the energy splitting are uncorrelated and thus its auto-correlation function can be described as $\langle \delta E(t') \delta E(t'') \rangle = \hbar^2 D_\varphi \delta(t' - t'')$, where D_φ^{-1} is a constant value that is called the dephasing time. Consequently, the dephasing rate D_φ can be calculated as

$$D_\varphi = \frac{1}{t \hbar^2} \int_0^t dt' \int_0^t dt'' \langle \delta E(t') \delta E(t'') \rangle = \frac{1}{t \hbar^2} \int_0^t dt' \int_0^t dt'' \frac{\sum_{n_{\text{ri}}} \langle n_{\text{ri}} | \delta E(t') \delta E(t'') | n_{\text{ri}} \rangle e^{-\epsilon_{n_{\text{ri}}}/T}}{\sum_{n_{\text{ri}}} e^{-\epsilon_{n_{\text{ri}}}/T}}, \quad (\text{S18})$$

where the ensemble average is taken over all the possible ripplon states and T is the liquid helium temperature.

As is the case for the spin relaxation, the dephasing process is described by the second-order perturbation theory. The energy fluctuation happens due to the virtual transitions to other orbital states where the electron feels a different magnetic field due to the vertical field gradient, whose Hamiltonian is W_z . Differently from the relaxation process, the time-averaged energy consumed or produced by the electron after the whole dephasing process is zero. Thereby, the thermally excited long-wavelength ripples are involved here. The one-ripple scattering cannot induce this energy-conserving process since it requires zero-energy consumption. Therefore, the two-ripple scattering is responsible for this process. Under the long-wavelength approximation, the Hamiltonian for the two-ripple scattering is written as [15]

$$H_{2\text{ri}}^K = \sum_{\mathbf{q}_1} \sum_{\mathbf{q}_2} \mathbf{q}_1 \mathbf{q}_2 Q_{\mathbf{q}_1} Q_{\mathbf{q}_2} (-\hat{K}_z) e^{I(\mathbf{q}_1 + \mathbf{q}_2)\mathbf{r}} (a_{\mathbf{q}_1} + a_{-\mathbf{q}_1}^\dagger) (a_{\mathbf{q}_2} + a_{-\mathbf{q}_2}^\dagger), \quad (\text{S19})$$

where $\hat{K}_z = \frac{\hbar^2}{2m_e} \partial_z^2$ [15]. The Hamiltonian which causes the energy fluctuation can be described as

$$H = H_{2\text{ri}}^K + W_z. \quad (\text{S20})$$

Taking Eq. (S20) as the perturbation term, the leading term in the second-order energy shift of the spin-up (spin-down) state is calculated as

$$\delta E_\sigma(t) \approx 2 \frac{(H_{2\text{ri}}^K)_{i,\beta} (W_z)_{\beta,i}}{E_{(m=0, n_r=0, n_z=1, \sigma)} - E_{(m=0, n_r=1, n_z=1, \sigma)}}. \quad (\text{S21})$$

The definition of the states i , and β here is $i = (n_r = 0, \sigma)$ and $\beta = (n_r = 1, \sigma)$, where $\sigma = \uparrow$ or \downarrow . Here we take into account only the $n_r = 0, 1$, $n_z = 1$, and $m = 0$ states. The contributions from the other states are much smaller, thus are ignored. The time-dependent energy fluctuation becomes

$$\delta E(t) \approx \frac{2 \langle \phi_{m=0, n_r=0, n_z=1} | H_{2\text{ri}}^K | \phi_{m=0, n_r=1, n_z=1} \rangle g \mu_B \frac{d^2 b_z}{dr^2} \langle \phi_{m=0, n_r=1, n_z=1} | r^2 | \phi_{m=0, n_r=0, n_z=1} \rangle}{E_{m=0, n_r=0, n_z=1} - E_{m=0, n_r=1, n_z=1}}. \quad (\text{S22})$$

By inserting the identity operator $\mathbf{I} = \sum_{n_r, n_z} | \phi_{m=0, n_r, n_z} \rangle \langle \phi_{m=0, n_r, n_z} |$, we obtain the following approximation:

$$\begin{aligned} & \langle \phi_{m=0, n_r=0, n_z=1} | H_{2\text{ri}}^K | \phi_{m=0, n_r=1, n_z=1} \rangle \\ & \approx \langle \phi_{m=0, n_r=0, n_z=1} | -\hat{K}_z | \phi_{m=0, n_r=0, n_z=1} \rangle \\ & \quad \times \sum_{\mathbf{q}_1} \sum_{\mathbf{q}_2} \mathbf{q}_1 \mathbf{q}_2 Q_{\mathbf{q}_1} Q_{\mathbf{q}_2} \langle \phi_{m=0, n_r=0, n_z=1} | e^{I(\mathbf{q}_1 + \mathbf{q}_2)\mathbf{r}} | \phi_{m=0, n_r=1, n_z=1} \rangle (a_{\mathbf{q}_1} + a_{-\mathbf{q}_1}^\dagger) (a_{\mathbf{q}_2} + a_{-\mathbf{q}_2}^\dagger). \end{aligned} \quad (\text{S23})$$

We numerically confirmed that the other terms are negligibly small. Using this approximation, we obtain the energy correlation function as

$$\begin{aligned} \delta E(t') \delta E(t'') & \approx \frac{4(g \mu_B \frac{d^2 b_z}{dr^2} \langle \phi_{m=0, n_r=1, n_z=1} | r^2 | \phi_{m=0, n_r=0, n_z=1} \rangle)^2}{(E_{n_r=0} - E_{n_r=1})^2} \left| \langle \phi_{m=0, n_r=0, n_z=1} | -\hat{K}_z | \phi_{m=0, n_r=0, n_z=1} \rangle \right|^2 \\ & \quad \times \sum_{\mathbf{q}_1, \mathbf{q}_2} \sum_{\tilde{\mathbf{q}}_1, \tilde{\mathbf{q}}_2} \mathbf{q}_1 \mathbf{q}_2 \tilde{\mathbf{q}}_1, \tilde{\mathbf{q}}_2 Q_{\mathbf{q}_1} Q_{\mathbf{q}_2} Q_{\tilde{\mathbf{q}}_1} Q_{\tilde{\mathbf{q}}_2} \\ & \quad \times \langle \phi_{m=0, n_r=0, n_z=1} | e^{I(\mathbf{q}_1 + \mathbf{q}_2)\mathbf{r}} | \phi_{m=0, n_r=1, n_z=1} \rangle \langle \phi_{m=0, n_r=0, n_z=1} | e^{I(\tilde{\mathbf{q}}_1 + \tilde{\mathbf{q}}_2)\mathbf{r}} | \phi_{m=0, n_r=1, n_z=1} \rangle \\ & \quad \times (a_{\mathbf{q}_1}(t') + a_{-\mathbf{q}_1}^\dagger(t')) (a_{\mathbf{q}_2}(t') + a_{-\mathbf{q}_2}^\dagger(t')) (a_{\mathbf{q}_1}(t'') + a_{-\mathbf{q}_1}^\dagger(t'')) (a_{\mathbf{q}_2}(t'') + a_{-\mathbf{q}_2}^\dagger(t'')), \end{aligned} \quad (\text{S24})$$

where $a_{\mathbf{q}}(t) = a_{\mathbf{q}}(0)e^{-I\omega_{\mathbf{q}}t}$. Plugging this into Eq. (S18) and taking the integral according to,

$$\int_0^t dt' \int_0^t dt'' \frac{\sum_{n_{\text{ri}}} \langle n_{\text{ri}} | (a_{\mathbf{q}_1}(t') + a_{-\mathbf{q}_1}^\dagger(t'))(a_{\mathbf{q}_2}(t') + a_{-\mathbf{q}_2}^\dagger(t'))(a_{\mathbf{q}_1}(t'') + a_{-\mathbf{q}_1}^\dagger(t''))(a_{\mathbf{q}_2}(t'') + a_{-\mathbf{q}_2}^\dagger(t'')) | n_{\text{ri}} \rangle e^{-\epsilon_{n_{\text{ri}}}/T}}{\sum_{n_{\text{ri}}} e^{-\epsilon_{n_{\text{ri}}}/T}} = t\pi(\bar{n}_{q_1} + 1)\bar{n}_{q_2}\delta(\omega_{q_1} - \omega_{q_2})\delta(\mathbf{q}_1 - \tilde{\mathbf{q}}_1)\delta(\mathbf{q}_2 - \tilde{\mathbf{q}}_2), \quad (\text{S25})$$

where $\bar{n}_q = (e^{\hbar\omega_q/T} - 1)^{-1}$ and $\omega_q = \sqrt{\alpha_{\text{He}}q^3/\rho_{\text{He}}}$, we obtain the dephasing rate as

$$D_\varphi \approx \frac{4\pi(g\mu_B \frac{d^2 b_z}{dr^2} l_0^2)^2}{\hbar^2(E_{n_r=0} - E_{n_r=1})^2} \left| \langle \phi_{m=0, n_r=0, n_z=1} | -\hat{K}_z | \phi_{m=0, n_r=0, n_z=1} \rangle \right|^2 \times \sum_{\mathbf{q}_1, \mathbf{q}_2} (\mathbf{q}_1 \mathbf{q}_2)^2 (Q_{\mathbf{q}_1} Q_{\mathbf{q}_2})^2 \left| \frac{|\mathbf{q}_1 + \mathbf{q}_2|^2 l_0^2}{4} e^{-|\mathbf{q}_1 + \mathbf{q}_2|^2 l_0^2/4} \right|^2 (\bar{n}_{q_1} + 1)\bar{n}_{q_2}\delta(\omega_{q_1} - \omega_{q_2}). \quad (\text{S26})$$

Here we used the expressions $\langle \phi_{m=0, n_r=1, n_z=1} | r^2 | \phi_{m=0, n_r=0, n_z=1} \rangle = l_0^2$ and $|\langle \phi_{m=0, n_r=0, n_z=1} | e^{I(\mathbf{q}_1 + \mathbf{q}_2)r} | \phi_{m=0, n_r=1, n_z=1} \rangle| = \left| \frac{|\mathbf{q}_1 + \mathbf{q}_2|^2 l_0^2}{4} e^{-|\mathbf{q}_1 + \mathbf{q}_2|^2 l_0^2/4} \right|$, which are valid for a harmonic confinement and is a good approximation for all the configurations shown in Fig. S5. By taking $x = ql_0$, Eq. (S26) is further reduced to

$$D_\varphi \approx \frac{\hbar^4 \left| \langle \phi_{m=0, n_r=0, n_z=1} | \partial_z^2 | \phi_{m=0, n_r=0, n_z=1} \rangle \right|^2 (\partial_r^2 f_{b_z} l_0^2)^2}{4m_e^2 48\pi^2 \rho_{\text{He}}^{1/2} \alpha_{\text{He}}^{3/2} l_0^{11/2}} \frac{1}{|\Delta f_{n_r=1 \rightarrow 0}|^2} \int_0^\infty dx \int_0^{2\pi} d\theta (\bar{n}_q + 1)\bar{n}_q x^{17/2} e^{-x^2(1-\cos\theta)} \cos^2\theta (1-\cos\theta)^2, \quad (\text{S27})$$

where $\partial_r^2 f_{b_z} = g\mu_B \frac{d^2 b_z}{dr^2}/h$ and $\Delta f_{n_r=1 \rightarrow 0} = (E_{n_r=1} - E_{n_r=0})/h$. Our numerical simulation shows that $\frac{\partial^2 b_z}{\partial r^2} = -0.0037 \text{ mT}/(\text{nm})^2$ at the position of the electron. Using these values, we calculated the dephasing rate as shown in Fig. S5.

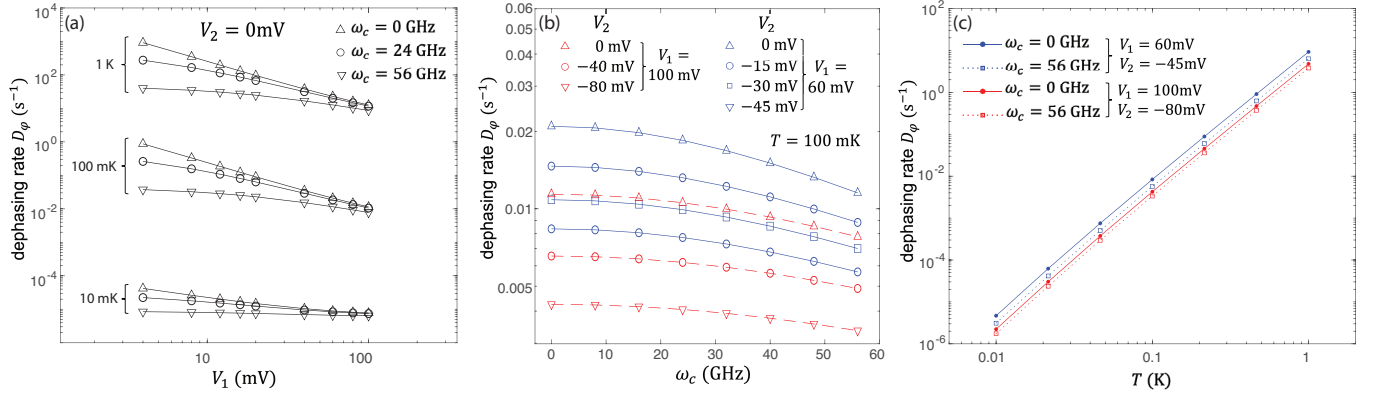


FIG. S5. Dephasing rate of the spin state as a function of V_1 with $V_2 = 0$ for different liquid helium temperatures and magnetic fields in (a), as a function of magnetic field (cyclotron frequency) for different voltage configurations and magnetic fields in (b) and as a function of temperature for different voltage configurations and magnetic fields in (c). As the dephasing process is dominated by the thermally excited ripplons, it has a strong temperature dependence shown in (c). The logarithm of the dephasing rate D_φ shows an almost linear relationship to the logarithm of the liquid helium temperature T .

D. Single-qubit gate fidelity

In order to calculate the gate fidelity, we used the Lindblad master equation [61]

$$\frac{d\rho}{dt} = -\frac{i}{\hbar}[H, \rho] + \frac{1}{2} \sum_i L(A_i)\rho \quad (\text{S28})$$

with $L(\Lambda)\rho = 2\Lambda\rho\Lambda^\dagger - \Lambda^\dagger\Lambda\rho - \rho\Lambda^\dagger\Lambda$. To calculate the single-qubit gate fidelity, we take the spin-state density operators as ρ , and we take $A_1 = \sqrt{\Gamma_{\text{relaxation}}}\lvert\downarrow\rangle\langle\uparrow\rvert$ and $A_2 = \sqrt{\frac{D_\varphi}{2}}\sigma_z$ as collapse operators. The Hamiltonian is described as $H = 2\pi f_{\text{Rabi}}\frac{\cos(\Theta)\sigma_x + \sin(\Theta)\sigma_y}{2}$ and Θ can be tuned by the AC electric field phase depending on the gates that we aim to apply. Here, we consider the case for the Rabi frequency $f_{\text{Rabi}} = 100$ MHz, the relaxation time: $1/\Gamma_{\text{relaxation}} = 50$ ms (see Sec. S.II B), and the dephasing time $1/D_\varphi = 100$ s (see Sec. S.II C). The average single-qubit gate fidelity is calculated to be

$$F_1 = \frac{1}{2} \sum_{i=0,1} \frac{1}{24} \sum_{j=1}^{24} \text{Tr}[\mathcal{C}_j^{\text{ideal}}(\rho_i)\mathcal{C}_j^{\text{real}}(\rho_i)], \quad (\text{S29})$$

where $\mathcal{C}_j^{\text{ideal}}(\rho_i)$ and $\mathcal{C}_j^{\text{real}}(\rho_i)$ denote the density operators obtained after applying one of the 24 Clifford gates in the single-qubit Clifford groups [62, 63] to the initial state ρ_i in the ideal case and real cases, respectively, and we take the average of two initial states $\rho_0 = \lvert\downarrow\rangle\langle\downarrow\rvert$ and $\rho_1 = \lvert\uparrow\rangle\langle\uparrow\rvert$ [64]. $\mathcal{C}_j^{\text{real}}(\rho_i)$ was numerically simulated using qutip.mesolve [65] and we obtained $F_1 > 99.9999\%$.

S.III. IMAGE CHARGE INDUCED ON THE CENTER ELECTRODE

In order to calculate the induced image charge on the center electrode, we applied the Shockley-Ramo theorem [66]. The theorem states that the charge Q on an electrode induced by a charge q is given by $Q = -q\phi_0(x)$, where $\phi_0(x)$ is the electric potential that would exist at the position x of charge q under the following circumstances: the selected electrode at unit potential, all other electrodes at zero potential and all charges are removed. Following this theorem, we run COMSOL simulation with 1 V to the center electrode and all the other electrodes grounded and then obtained the electric potential V_e at the position of the electron. The induced image charge on the center electrode by the electron is calculated to be $\frac{V_e}{1\text{V}}e$.

S.IV. TWO-QUBIT GATE

A. Screening effect on the Coulomb interaction

It is important to discuss the effect of screening of the Coulomb interaction between electrons by the conducting electrodes. Here, we consider the case where electron A and electron B are separated by a distance d along the x axis and their positions along the z axis are given by z_A and z_B , respectively. The electrode is an infinitely large plate covered with liquid helium of depth d_{He} , as shown in Fig. S6(a). The potential created by the Coulomb interaction of the two electrons is written as $U_C = \frac{e^2}{4\pi\epsilon_0} \frac{1}{\sqrt{d^2 + (z_B - z_A)^2}}$. When the helium depth is small enough, the electrons are so close to the electrode that the interaction between the image charge induced on the electrode and the adjacent electron is non-negligible (the screening effect). In this case, the potential created by the Coulomb interaction of the two electrons is reformulated as $U_C = \frac{e^2}{4\pi\epsilon_0} \left(\frac{1}{\sqrt{d^2 + (z_B - z_A)^2}} - \frac{1}{\sqrt{d^2 + (2d_{\text{He}} + z_B + z_A)^2}} \right)$. With $d = 0.88 \mu\text{m}$, $d_{\text{He}} = 140$ nm, the Coulomb interaction becomes 10^{-6} times smaller due to the screening effect, which means a much lower temperature is required for the electrons to form a Wigner crystal.

Although the screening effect diminishes the Coulomb interaction drastically in terms of formation of a Wigner crystal when $d_{\text{He}} \ll d$, it may even enhance the electric dipole-dipole interaction [41]. The leading term of the Coulomb interaction that contributes to the electric dipole-dipole interaction without the screening effect is $\frac{e^2}{4\pi\epsilon_0} \frac{z_A z_B}{d^3}$ and the corresponding Hamiltonian of the electric dipole-dipole interaction W' is given in the main text. The leading term of the Coulomb interaction from the screening effect is $\frac{e^2}{4\pi\epsilon_0} \frac{z_A z_B (d^2 - 8d_{\text{He}})}{D^5}$ with $D = \sqrt{d^2 + 4d_{\text{He}}^2}$. Thus, the enhancement factor acquired by the screening effect is $\kappa = 1 + \frac{d^3 (d^2 - 8d_{\text{He}})}{D^5}$ and is shown in Fig. S6(b). The electric dipole-dipole interaction is doubled when $d_{\text{He}} \ll d$ and its minimum value ≈ 0.8 is reached at $d_{\text{He}} \approx d/2$.

B. Controlled-phase gate

As discussed in the main text, we realize a two-qubit gate for the spin states by applying resonant microwaves to the Rydberg states of target qubits. This can be achieved because we can excite the Rydberg states of a target

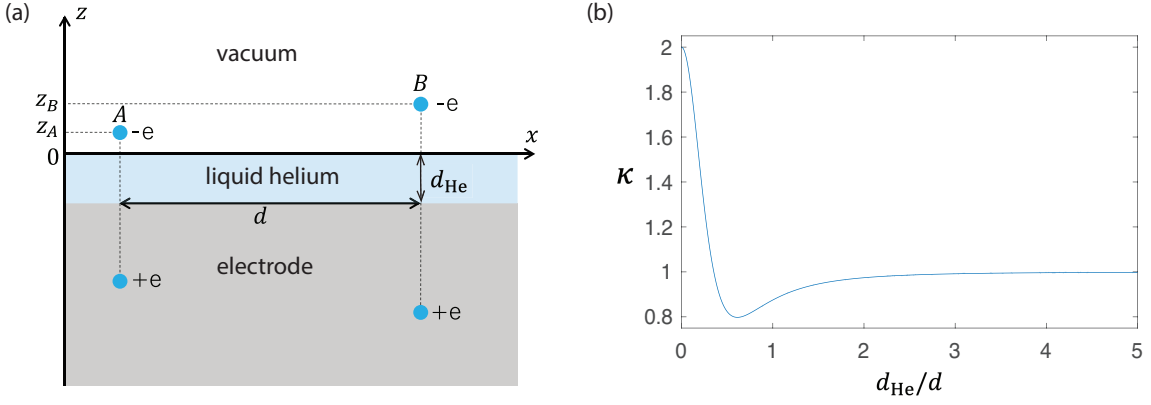


FIG. S6. (a) Electron A and electron B are separated by d horizontally. An electron and the induced image charge on the electrode are equally distant from the surface of the electrode. The value of the image charge is equal to the elementary charge. z_A and z_B denote vertical positions of electrons A and B, respectively. The figure depicts the case where electron A is in the Rydberg-ground state and electron B is in the Rydberg-1st-excited state. (b) The enhancement factor acquired by the screening effect in the electric dipole-dipole interaction as a function of the helium depth d_{He} normalized by d .

qubit (qubit B for the first MW pulse in Fig. 3(b) of the main text) depending on the spin state of the target qubit thanks to the Rydberg-spin interaction and depending on the Rydberg state of an adjacent qubit (qubit A for the first MW pulse) thanks to the electric dipole-dipole interaction. However, when the Rydberg transition energy difference between different spin states of the target qubit or between different Rydberg states of the adjacent qubit is small compared to the transition rate, we cannot ignore a portion of the Rydberg state being excited even when the spin state or the Rydberg state of the adjacent qubit is in the unintended states. Furthermore, we should also take into account the phase acquired for the target qubit in unintended states through the Rydberg-spin interaction and the electric dipole-dipole interaction. Note that making $|\Delta R_i - \Delta R_j| \gg \hbar f_1$ is trivial thanks to the DC Stark shift and thus we do not have to consider off-resonant excitation of the unintended qubits.

Now we consider the phase acquired during the three MW pulse sequences shown in Fig. 3(b) of the main text. For the sake of obtaining a high two-qubit gate fidelity, we consider the case of $\Delta b = 4J = \sqrt{15}\hbar\Omega_1$. When the microwave resonant with the Rydberg transition of qubit B is applied, the Hamiltonian of qubit B is given by

$$H = \Omega_1 \cos(\omega_{\text{MW}}) s_x^B + \frac{1}{2} \Delta R_B s_z^B - \frac{1}{2} \Delta b s_z^B \sigma^B + J s_z^A s_z^B, \quad (\text{S30})$$

where the spin-only terms are neglected.

The first MW pulse : For the first MW pulse, the microwave frequency is set to $\omega_{\text{MW}}/2\pi = f_{0, \text{RydbergB}}^{n_z^A=1, \sigma^B=\downarrow}$. The Hamiltonian in the rotating frame of the angular frequency ω_{MW} becomes

$$H = \frac{\hbar\Omega_1}{2} s_x^B - \frac{\Delta b}{2} s_z^B |\uparrow^B\rangle \langle \uparrow^B| + 2J |2^A\rangle \langle 2^A| s_z^B. \quad (\text{S31})$$

The time duration of the first MW pulse is set so that it acts as a π pulse for the Rydberg state when the initial state of the spin state is $|\downarrow^B\rangle$. This rotation can be denoted as $R_x^B(\pi)$. Then, the Rydberg state of qubit B after the first pulse is $-I|2^B\rangle$. When the initial spin state of B is $|\uparrow^B\rangle$, there is a detuning of $-\Delta b$. In this situation, as seen in footnote [67], the first pulse acts as $R_{(\cos v_1, 0, \sin v_1)}^B(4\pi)$ with $v_1 = \arctan \frac{-\Delta b}{\hbar\Omega_1} = \arctan(-\sqrt{15})$. Then, the Rydberg state of qubit B after the first pulse is $|1^B\rangle$ (unchanged due to the 4π rotation).

The second MW pulse : For the second MW pulse, the microwave frequency is set to $\omega_{\text{MW}}/2\pi = f_{0, \text{RydbergA}}^{n_z^B=2, \sigma^A=\downarrow}$. The Hamiltonian on the rotating frame of the angular frequency ω_{MW} becomes

$$H = \frac{\hbar\Omega_1}{2} s_x^A - \frac{\Delta b}{2} s_z^A |\uparrow^A\rangle \langle \uparrow^A| - 2J s_z^A |1^B\rangle \langle 1^B|. \quad (\text{S32})$$

The second pulse acts as a 2π pulse when the spin state of qubit A is $|\downarrow^A\rangle$ and the Rydberg state of qubit B is $|2^B\rangle$. After this pulse, the phase is multiplied by -1 . When the spin state of qubit A is $|\uparrow^A\rangle$ or the Rydberg state of qubit B is $|1^B\rangle$, there is a detuning of $-\Delta b$ or $-4J$. That is, the second pulse acts as $R_{(\cos v_1, 0, \sin v_1)}^A(8\pi)$. Then, the Rydberg state

of qubit A after the second pulse stays the same as before the second pulse (unchanged due to the 8π rotation). When the spin state of qubit A is $|\uparrow^A\rangle$ and the Rydberg state of qubit B is $|1^B\rangle$ there is a detuning of $-\Delta b - 4J = -2\sqrt{15}\Omega_1$. We can describe the rotation here as $R_{(\cos v_2, 0, \sin v_2)}^A(\sqrt{61} \cdot 2\pi)$ with $v_2 = \arctan(-2\Delta b/\Omega_1) = \arctan(-2\sqrt{15})$. The state after the second pulse is

$$\left(\cos\left(\frac{\sqrt{61} \cdot 2\pi}{2}\right) s_0 - I \sin\left(\frac{\sqrt{61} \cdot 2\pi}{2}\right) (s_x \cos v_2 + s_z \sin v_2) \right) |1^A\rangle = (0.8275 + 0.5568I) |1^A\rangle + 0.0719I |2^A\rangle, \quad (\text{S33})$$

where s_0 is the identity operator.

The third MW pulse : The third pulse works in the same way as the first pulse. The only difference is that the phase of the third pulse is different from the first pulse by π . The Hamiltonian on the rotating frame of the angular frequency ω_{MW} is

$$H = -\frac{\hbar\Omega_1}{2} s_x^B - \frac{\Delta b}{2} s_z^B |\uparrow^B\rangle \langle \uparrow^B| + 2J |2^A\rangle \langle 2^A| s_z^B. \quad (\text{S34})$$

Note that when the Rydberg state of A is $|2^A\rangle$ and the spin state of B is $|\uparrow^B\rangle$, the detuning is $-\Delta b + 4J = 0$. Thus, the rotation is described as $R_{-x}^B(\pi)$. In Fig. S7, we summarize how the states evolve during the three pulses.

		$f_{0, \text{Rydberg B}}^{n_z^A=1, \sigma^B=\downarrow}$	$f_{0, \text{Rydberg A}}^{n_z^B=2, \sigma^A=\downarrow}$	$f_{0, \text{Rydberg B}}^{n_z^A=1, \sigma^B=\downarrow}$	time \rightarrow	
$ \sigma^A \sigma^B\rangle$	$ n_z^A n_z^B\rangle$	π_x	2π	$\pi_{\bar{x}}$	$ n_z^A n_z^B\rangle$	$ n_z^A n_z^B\rangle$
$ \uparrow\uparrow\rangle$	$ 11\rangle$	$R_{(\cos v_1, 0, \sin v_1)}^B(4\pi)$	$R_{(\cos v_2, 0, \sin v_2)}^A(\sqrt{61} \cdot 2\pi)$	$R_{(\cos v_1, 0, \sin v_1)}^B(4\pi)$	$(0.8275 + 0.5568I) 11\rangle + i0.0719 21\rangle$	$(0.8275 + 0.5568I) 11\rangle - 0.0719 22\rangle$
$ \downarrow\downarrow\rangle$	$ 11\rangle$	$R_{(\cos v_1, 0, \sin v_1)}^B(4\pi)$	$R_{(\cos v_2, 0, \sin v_2)}^A(8\pi)$	$R_{(\cos v_1, 0, \sin v_1)}^B(4\pi)$	$ 11\rangle$	$ 11\rangle$
$ \uparrow\downarrow\rangle$	$ 11\rangle$	$R_x^B(\pi)$	$R_x^A(2\pi)$	$R_{-x}^B(\pi)$	$-I 12\rangle$	$ 11\rangle$
$ \downarrow\uparrow\rangle$	$ 11\rangle$	$R_x^B(\pi)$	$R_x^A(2\pi)$	$R_{-x}^B(\pi)$	$I 12\rangle$	$- 11\rangle$

FIG. S7. How the qubit states evolve during the three MW pulses when $\Delta b = 4J = \sqrt{15}\hbar\Omega_1$.

As seen in Fig. S7, the total operation of a set of three pulses is described as

$$\begin{pmatrix} 0.9974e^{0.1885I\pi} & 0 & 0 & 0 \\ 0 & 1 & 0 & 0 \\ 0 & 0 & 1 & 0 \\ 0 & 0 & 0 & -1 \end{pmatrix}. \quad (\text{S35})$$

Here, the Rydberg-excited states are treated as leakage states and the space is defined by the spin states of qubits A and B: $|\uparrow\uparrow\rangle$, $|\downarrow\downarrow\rangle$, $|\uparrow\downarrow\rangle$, and $|\downarrow\uparrow\rangle$. Eq. (S35) is equivalent to

$$\begin{pmatrix} e^{0.1885I\pi} & 0 & 0 & 0 \\ 0 & 1 & 0 & 0 \\ 0 & 0 & 1 & 0 \\ 0 & 0 & 0 & -1 \end{pmatrix} \quad (\text{S36})$$

with a small error due to the leakage to $|2^A 2^B\rangle$. Eq. (S36) can be transformed into a controlled- (1.1885π) gate, $CP_{1.1885\pi} = |\uparrow^A\rangle \langle \uparrow^A| \otimes \sigma_0^B + |\downarrow^A\rangle \langle \downarrow^A| \otimes R_z^B(1.1885\pi)$, where σ_0 is the identity operator, by applying single-qubit z -rotations and adding some global phases.

C. Controlled- π gate

Following [68, 69], we found that a controlled- $(-\Theta)$ gate, $CP_{-\Theta}$, can be constructed out of the two times of a controlled- $(\pi + \Theta)$ gate, $CP_{\pi+\Theta}$, and single-qubit gates, for $0 < \Theta < \frac{2}{3}\pi$. Knowing that a controlled- π gate can be realized by $CP_{\pi} = CP_{\pi+\Theta}CP_{-\Theta}$, CP_{π} can be constructed out of the three times of $CP_{\pi+\Theta}$ and single-qubit gates. More concretely, we found

$$CP_{1.1885\pi}R_y^{B\dagger}(\Xi_2)R_z^{B\dagger}(\Xi_1)CP_{1.1885\pi}R_x^{B\dagger}(\Xi_0)CP_{1.1885\pi}R_x^B(\Xi_0)R_z^B(\Xi_1)R_y^B(\Xi_2) = \begin{pmatrix} 1 & 0 & 0 & 0 \\ 0 & 1 & 0 & 0 \\ 0 & 0 & -I & 0 \\ 0 & 0 & 0 & I, \end{pmatrix} \quad (\text{S37})$$

with $\Xi_0 = 0.9014\pi$, $\Xi_1 = 0.0943\pi$, and $\Xi_2 = 0.4855\pi$ as one of the solutions. Eq. (S37) is equal to a controlled- (π) gate, $CP_{\pi} = |\uparrow^A\rangle\langle\uparrow^A| \otimes \sigma_0^B + |\downarrow^A\rangle\langle\downarrow^A| \otimes R_z^B(\pi)$.

D. Two-qubit gate fidelity

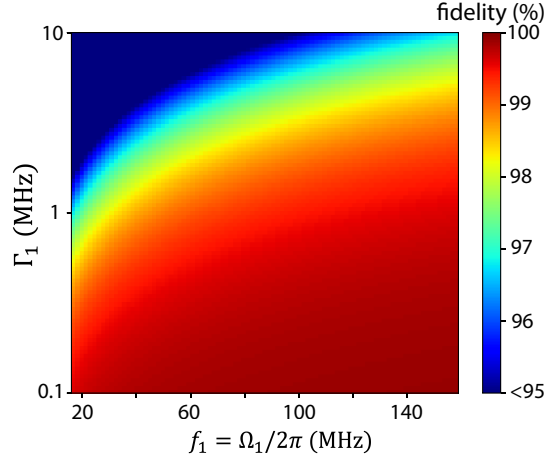


FIG. S8. Fidelity of the controlled- (1.1885π) gate realized by applying the three MW pulses (Fig. S7) with $\Delta b = 4J = \sqrt{15}\hbar\Omega_1$.

In order to calculate the two-qubit gate fidelity, we use the Lindblad master equation (Eq. (S28)). Here, ρ is the density operator of both the spin states and the two-lowest Rydberg states of qubits A and B. We take $A_1 = \sqrt{\Gamma_1}|1^A\rangle\langle 2^A|$ and $A_2 = \sqrt{\Gamma_1}|1^B\rangle\langle 2^B|$ as collapse operators where $\Gamma_1 = 1$ MHz is the relaxation rate of the Rydberg state [28, 29, 70]. The Rydberg dephasing rate [15, 22], the spin relaxation rate, and the spin dephasing rate are much smaller than Γ_1 , and thus can be ignored. The average gate fidelity of the controlled- (1.1885π) is calculated to be

$$F_2 = \frac{1}{16} \left[4 + \frac{1}{5} \sum_{i=1}^{15} \text{Tr}[\mathcal{CP}_{1.1885\pi}^{\text{ideal}}(\rho_i^{\text{spin}})\mathcal{CP}_{1.1885\pi}^{\text{real}}(\rho_i^{\text{spin}})] \right]. \quad (\text{S38})$$

Here ρ_i^{spin} is the Kronecker product of Pauli matrices of the spin states:

$$\rho_i^{\text{spin}} = \sigma_{\mu}^A \otimes \sigma_{\nu}^B, \quad \mu, \nu = 0, x, y, z, \quad (\text{S39})$$

and $\sigma_0^A \otimes \sigma_0^B$ is excluded from the sum of Eq. (S38) [71]. $\mathcal{CP}_{1.1885\pi}^{\text{ideal}}(\rho_i^{\text{spin}})$ and $\mathcal{CP}_{1.1885\pi}^{\text{real}}(\rho_i^{\text{spin}})$ denote the density operators obtained after applying the controlled- (1.1885π) gate to the initial state ρ_i^{spin} in the ideal and real cases, respectively. We obtained $\mathcal{CP}_{1.1885\pi}^{\text{real}}(\rho_i^{\text{spin}})$ by numerically calculating $\mathcal{CP}_{1.1885\pi}^{\text{real}}(\rho_i^{\text{spin}} \otimes |1^A\rangle\langle 1^A| \otimes |1^B\rangle\langle 1^B|)$ using qutip.mesolve [65] and tracing over the Rydberg states. In addition to the leakage that already appears in Eq. (S35), the Rydberg relaxation degrades the fidelity. For the case considered in the main text, $\Delta b = 4J = \sqrt{15}\hbar\Omega_1 = 2\pi \cdot 137$ MHz (i.e., $f_1 = 35.5$ MHz), we obtained $F_2 = 98.5\%$. As seen in Sec. S.IV C, the controlled- (π) gate can be realized by applying the controlled- (1.1885π) gate three times and single-qubit gates several times. The single-qubit

gate fidelity is much higher than the two-qubit gate fidelity and therefore the controlled- (π) gate fidelity is dominated by the controlled- (1.1885π) gate fidelity and thus is calculated by F_2^3 . Fig. S8 shows the fidelity of the controlled- (1.1885π) gate for different Rabi frequencies f_1 and relaxation rates Γ_1 of the Rydberg state with $\Delta b = 4J = \sqrt{15}\hbar\Omega_1$. We cannot simply increase f_1 because of the constraint $\Delta b = 4J = \sqrt{15}\hbar\Omega_1$ but should increase the field gradient and the Coulomb interaction at the same time. The field gradient can be increased by choosing a different ferromagnetic material that has a higher saturation magnetic field than Co, such as CoFe ($\approx 5\%$ higher) [57] or Gd ($\approx 40\%$ higher) [72]. Alternatively, we can make the helium depth thinner but the Rydberg transition energy becomes higher. Sending a higher-frequency MW is more costly and difficult. The Coulomb interaction can be made larger by making the distance between electrons smaller. There are some limits on the electron density set by the hydrodynamic instability but the distance between electrons can be made as small as $0.1 \mu\text{m}$ [8]. Γ_1 was theoretically estimated and experimentally measured to be ≈ 1 MHz for a liquid helium temperature lower than 100 mK [28, 29, 70]. According to Ref. [28, 70], Γ_1 is limited by the two-ripplon emission of short-wavelength capillary waves and the entire discussion in this manuscript follows this theory, unless otherwise states. However, other theoretical studies claim that Γ_1 should be limited by one-ripplon scattering and < 0.01 MHz [15, 30]. With $\Gamma_1 = 0.1$ MHz (0.01 MHz) and $f_1 = 35.5$ MHz, the controlled- (π) gate (CZ gate) fidelity of $\approx 99.3\%$ ($\approx 99.7\%$) can be achieved.

S.V. READ-OUT OF THE QUBIT STATE

The density operator of the two-lowest Rydberg states can be written as $\rho = \frac{1}{2}s_0 + \frac{1}{2}\vec{s} \cdot \vec{r}$ where $\vec{s} = (s_x, s_y, s_z)$ and $\vec{r} = (r_x, r_y, r_z)$. The time evolution of this density operator under H_R of the main text can be described by the Bloch equations as

$$\begin{aligned}\frac{dr_x}{dt} &= -\frac{1}{T_2}r_x - \Delta\omega(t)r_y \\ \frac{dr_y}{dt} &= -\frac{1}{T_2}r_y + \Delta\omega(t)r_x - \omega_1r_z \\ \frac{dr_z}{dt} &= -\frac{1}{T_1}(r_z + 1) + \omega_1r_y.\end{aligned}$$

We numerically solved the above differential equations with $\omega(t) = \Delta\omega_0 + 2\pi A_m \cos(\omega_m t)$ and calculated $\rho_{22}(t) = \frac{r_z(t)+1}{2}$. From this, we obtain the in-phase component of ρ_{22} , which is plotted in Fig. 4 of the main text.

-
- [1] A. G. Fowler, M. Mariantoni, J. M. Martinis, and A. N. Cleland, Surface codes: Towards practical large-scale quantum computation, *Phys. Rev. A* **86**, 032324 (2012).
 - [2] D. Wineland, P. Ekstrom, and H. Dehmelt, Monoelectron oscillator, *Phys. Rev. Lett.* **31**, 1279 (1973).
 - [3] C. Matthiesen, Q. Yu, J. Guo, A. M. Alonso, and H. Häffner, Trapping electrons in a room-temperature microwave paul trap, *Phys. Rev. X* **11**, 011019 (2021).
 - [4] Q. Yu, A. M. Alonso, J. Caminiti, K. M. Beck, R. T. Sutherland, D. Leibfried, K. J. Rodriguez, M. Dhital, B. Hemmerling, and H. Häffner, Feasibility study of quantum computing using trapped electrons, *Phys. Rev. A* **105**, 022420 (2022).
 - [5] X. Zhou, G. Koolstra, X. Zhang, G. Yang, X. Han, B. Dizdar, X. Li, R. Divan, W. Guo, K. W. Murch, D. I. Schuster, and D. Jin, Single electrons on solid neon as a solid-state qubit platform, *Nature* **605**, 46 (2022).
 - [6] X. Zhou, X. Li, Q. Chen, G. Koolstra, G. Yang, B. Dizdar, X. Han, X. Zhang, D. I. Schuster, and D. Jin, Electron charge qubits on solid neon with 0.1 millisecond coherence time, (2022), arXiv:2210.12337.
 - [7] K. Shirahama, S. Ito, H. Suto, and K. Kono, Surface study of liquid³He using surface state electrons, *J. Low Temp. Phys.* **101**, 439 (1995).
 - [8] D. Marty, Stability of two-dimensional electrons on a fractionated helium surface, *J. Phys. C: Solid State Phys.* **19**, 6097 (1986).
 - [9] E. Rousseau, Y. Mukharsky, D. Ponarine, O. Avenel, and E. Varoquaux, Trapping Electrons in Electrostatic Traps over the Surface of 4He, *J. Low Temp. Phys.* **148**, 193 (2007).
 - [10] H. Ikegami, H. Akimoto, and K. Kono, Nonlinear transport of the wigner solid on superfluid 4He in a channel geometry, *Phys. Rev. Lett.* **102**, 046807 (2009).
 - [11] S. Zou and D. Konstantinov, Image-charge detection of the rydberg transition of electrons on superfluid helium confined in a microchannel structure, *New J. Phys.* **24**, 103026 (2022).
 - [12] D. G. Rees, I. Kuroda, C. A. Marrache-Kikuchi, M. Höfer, P. Leiderer, and K. Kono, Point-contact transport properties of strongly correlated electrons on liquid helium, *Phys. Rev. Lett.* **106**, 026803 (2011).
 - [13] D. G. Rees, H. Totsuji, and K. Kono, Commensurability-dependent transport of a wigner crystal in a nanoconstriction, *Phys. Rev. Lett.* **108**, 176801 (2012).

- [14] P. M. Platzman and M. I. Dykman, A potentially realizable quantum computer., *Science* **261**, 1569 (1993).
- [15] M. I. Dykman, P. M. Platzman, and P. Seddighrad, Qubits with electrons on liquid helium, *Phys. Rev. B* **67**, 155402 (2003).
- [16] S. A. Lyon, Spin-based quantum computing using electrons on liquid helium, *Phys. Rev. A* **74**, 052338 (2006).
- [17] D. I. Schuster, A. Fragner, M. I. Dykman, S. A. Lyon, and R. J. Schoelkopf, Proposal for Manipulating and Detecting Spin and Orbital States of Trapped Electrons on Helium Using Cavity Quantum Electrodynamics, *Phys. Rev. Lett.* **105**, 040503 (2010).
- [18] G. Papageorgiou, P. Glasson, K. Harrabi, V. Antonov, E. Collin, P. Fozooni, P. G. Frayne, M. J. Lea, D. G. Rees, and Y. Mukharsky, Counting Individual Trapped Electrons on Liquid Helium, *Appl. Phys. Lett.* **86**, 153106 (2005).
- [19] F. R. Bradbury, M. Takita, T. M. Gurrieri, K. J. Wilkel, K. Eng, M. S. Carroll, and S. A. Lyon, Efficient clocked electron transfer on superfluid helium, *Phys. Rev. Lett.* **107**, 266803 (2011).
- [20] G. Koolstra, G. Yang, and D. I. Schuster, Coupling a single electron on superfluid helium to a superconducting resonator, *Nat. Commun.* **10**, 5323 (2019).
- [21] H. Byeon, K. Nasyedkin, J. R. Lane, N. R. Beysengulov, L. Zhang, R. Loloee, and J. Pollanen, Piezoacoustics for precision control of electrons floating on helium, *Nat. Commun.* **12**, 4150 (2021).
- [22] P. M. Platzman and M. I. Dykman, Quantum Computing with Electrons Floating on Liquid Helium, *Science* **284**, 1967 (1999).
- [23] Y. Monarkha and K. Kono, Two-Dimensional Interface Electron Systems (2004) pp. 1–63.
- [24] L. Trifunovic, O. Dial, M. Trif, J. R. Wootton, R. Abebe, A. Yacoby, and D. Loss, Long-Distance Spin-Spin Coupling via Floating Gates, *Phys. Rev. X* **2**, 011006 (2012).
- [25] N. Samkharadze, G. Zheng, N. Kalhor, D. Brousse, A. Sammak, U. C. Mendes, A. Blais, G. Scappucci, and L. M. K. Vandersypen, Strong spin-photon coupling in silicon., *Science* **359**, 1123 (2018).
- [26] M. Veldhorst, H. G. J. Eenink, C. H. Yang, and A. S. Dzurak, Silicon CMOS architecture for a spin-based quantum computer, *Nature Communications* **8**, 1766 (2017).
- [27] T. D. Ladd, D. Maryenko, Y. Yamamoto, E. Abe, and K. M. Itoh, Coherence time of decoupled nuclear spins in silicon, *Phys. Rev. B* **71**, 1 (2005).
- [28] Y. P. Monarkha, S. S. Sokolov, A. V. Smorodin, and N. Studart, Decay of excited surface electron states in liquid helium and related relaxation phenomena induced by short-wavelength ripplons, *Low Temp. Phys.* **36**, 565 (2010).
- [29] E. Kawakami, A. Elarabi, and D. Konstantinov, Relaxation of the excited rydberg states of surface electrons on liquid helium, *Phys. Rev. Lett.* **126**, 106802 (2021).
- [30] M. I. Dykman, O. Asban, Q. Chen, D. Jin, and S. A. Lyon, Spin dynamics in quantum dots on liquid helium, (2022), arXiv:2212.10683.
- [31] M. Zhang and L. F. Wei, Spin-orbit couplings between distant electrons trapped individually on liquid helium, *Phys. Rev. B* **86**, 205408 (2012).
- [32] Y. Tokura, W. G. van der Wiel, T. Obata, and S. Tarucha, Coherent Single Electron Spin Control in a Slanting Zeeman Field, *Phys. Rev. Lett.* **96**, 047202 (2006).
- [33] C. C. Grimes and G. Adams, Evidence for a liquid-to-crystal phase transition in a classical, two-dimensional sheet of electrons, *Phys. Rev. Lett.* **42**, 795 (1979).
- [34] P. Krantz, A. Bengtsson, M. Simoen, S. Gustavsson, V. Shumeiko, W. D. Oliver, C. M. Wilson, P. Delsing, and J. Bylander, Single-shot read-out of a superconducting qubit using a josephson parametric oscillator, *Nat. Commun.* **7**, 11417 (2016).
- [35] M. Pioro-Ladrière, T. Obata, Y. Tokura, Y.-S. Shin, T. Kubo, K. Yoshida, T. Taniyama, and S. Tarucha, Electrically driven single-electron spin resonance in a slanting Zeeman field, *Nat. Phys.* **4**, 776 (2008).
- [36] E. Kawakami, P. Scarlino, D. R. Ward, F. R. Braakman, D. E. Savage, M. G. Lagally, M. Friesen, S. N. Coppersmith, M. A. Eriksson, and L. M. K. Vandersypen, Electrical control of a long-lived spin qubit in a Si/SiGe quantum dot., *Nat. Nanotechnol.* **9**, 666–670 (2014).
- [37] M. F. Gonzalez-Zalba, S. Barraud, A. J. Ferguson, A. C. Betz, and P. Delsing, Probing the limits of gate-based charge sensing, *Nat. Commun.* **6**, 6084 (2015).
- [38] E. Kawakami, A. Elarabi, and D. Konstantinov, Image-charge detection of the rydberg states of surface electrons on liquid helium, *Phys. Rev. Lett.* **123**, 086801 (2019).
- [39] Virginia Diodes, Inc, <https://www.vadiodes.com/en/frequency-multipliers>.
- [40] Y. P. Monarkha and S. S. Sokolov, Decay rate of the excited states of surface electrons over liquid helium, *J. Low Temp. Phys.* **148**, 157 (2007).
- [41] M. Lea, P. Frayne, and Y. Mukharsky, Could we Quantum Compute with Electrons on Helium?, *Fortschritte der Physik* **48**, 1109 (2000).
- [42] J. I. Cirac and P. Zoller, Quantum computations with cold trapped ions, *Phys. Rev. Lett.* **74**, 4091 (1995).
- [43] M. Saffman, T. G. Walker, and K. Mølmer, Quantum information with rydberg atoms, *Rev. Mod. Phys.* **82**, 2313 (2010).
- [44] S.-L. Su, E. Liang, S. Zhang, J.-J. Wen, L.-L. Sun, Z. Jin, and A.-D. Zhu, One-step implementation of the rydberg-rydberg-interaction gate, *Phys. Rev. A* **93**, 012306 (2016).
- [45] S.-L. Su, Y. Tian, H. Z. Shen, H. Zang, E. Liang, and S. Zhang, Applications of the modified rydberg antiblockade regime with simultaneous driving, *Phys. Rev. A* **96**, 042335 (2017).
- [46] X.-F. Shi, Rydberg quantum gates free from blockade error, *Phys. Rev. Applied* **7**, 064017 (2017).
- [47] F. Motzoi, J. M. Gambetta, P. Rebentrost, and F. K. Wilhelm, Simple pulses for elimination of leakage in weakly nonlinear qubits, *Phys. Rev. Lett.* **103**, 110501 (2009).
- [48] L. Landau, An ultrasensitive radio-frequency single-electron transistor working up to 4.2 k, *Phys. Z. Sowjetunion* **2** (1932).
- [49] C. Zener, Non-Adiabatic Crossing of Energy Levels, *Proceedings of the Royal Society A: Mathematical, Physical and Engineering Sciences*

- [50] S. Shevchenko, S. Ashhab, and F. Nori, Landau–Zener–Stückelberg interferometry, *Physics Reports* **492**, 1 (2010).
- [51] H. Brenning, S. Kafanov, T. Duty, S. Kubatkin, and P. Delsing, An ultrasensitive radio-frequency single-electron transistor working up to 4.2 k, *J. Appl. Phys.* **100**, 114321 (2006).
- [52] P. Apostolidis, B. J. Villis, J. F. Chittock-Wood, A. Baumgartner, V. Vesterinen, S. Simbierowicz, J. Hassel, and M. R. Buitelaar, Quantum paraelectric varactors for radio-frequency measurements at mk temperatures, (2020), arXiv:2007.03588.
- [53] V. B. Braginsky and F. Y. Khalili, Quantum nondemolition measurements: the route from toys to tools, *Rev. Mod. Phys.* **68**, 1 (1996).
- [54] H. Ball, T. M. Stace, S. T. Flammia, and M. J. Biercuk, Effect of noise correlations on randomized benchmarking, *Phys. Rev. A* **93**, 022303 (2016).
- [55] P. Glasson, G. Papageorgiou, K. Harrabi, D. G. Rees, V. Antonov, E. Collin, P. Fozooni, P. G. Frayne, Y. Mukharsky, and M. J. Lea, Trapping single electrons on liquid helium, *J. Phys. Chem. Solids* **66**, 1539 (2005).
- [56] G. Petersen, E. A. Hoffmann, D. Schuh, W. Wegscheider, G. Giedke, and S. Ludwig, Large nuclear spin polarization in gate-defined quantum dots using a single-domain nanomagnet, *Phys. Rev. Lett.* **110**, 177602 (2013).
- [57] D. Lachance-Quirion, J. Camirand Lemyre, L. Bergeron, C. Sarra-Bournet, and M. Pioro-Ladrière, Magnetometry of micro-magnets with electrostatically defined hall bars, *Appl. Phys. Lett.* **107**, 223103 (2015).
- [58] D. R. W. Yost, M. E. Schwartz, J. Mallek, D. Rosenberg, C. Stull, J. L. Yoder, G. Calusine, M. Cook, R. Das, A. L. Day, E. B. Golden, D. K. Kim, A. Melville, B. M. Niedzielski, W. Woods, A. J. Kerman, and W. D. Oliver, Solid-state qubits integrated with superconducting through-silicon vias, *npj Quantum Information* **6**, 1 (2020).
- [59] S. Tamate, Y. Tabuchi, and Y. Nakamura, Toward realization of scalable packaging and wiring for large-scale superconducting quantum computers, *IEICE Transactions on Electronics* **E105.C**, 290 (2022).
- [60] L. Jacak, A. Wójs, and P. Hawrylak, *Quantum Dots* (Springer Berlin Heidelberg, 1998).
- [61] G. Lindblad, On the generators of quantum dynamical semigroups, *Commun. Math. Phys.* **48**, 119 (1976).
- [62] E. Knill, D. Leibfried, R. Reichle, J. Britton, R. B. Blakestad, J. D. Jost, C. Langer, R. Ozeri, S. Seidelin, and D. J. Wineland, Randomized benchmarking of quantum gates, *Phys. Rev. A* **77**, 012307 (2008).
- [63] J. Emerson, R. Alicki, and K. Życzkowski, Scalable noise estimation with random unitary operators, *J. Opt. B Quantum Semiclassical Opt.* **7**, S347 (2005).
- [64] J. T. Muhonen, A. Laucht, S. Simmons, J. P. Dehollain, R. Kalra, F. E. Hudson, S. Freer, K. M. Itoh, D. N. Jamieson, J. C. McCallum, A. S. Dzurak, and A. Morello, Quantifying the quantum gate fidelity of single-atom spin qubits in silicon by randomized benchmarking, *J. Phys. Condens. Matter* **27**, 154205 (2015).
- [65] J. R. Johansson, P. D. Nation, and F. Nori, Qutip 2: A python framework for the dynamics of open quantum systems, *Comput. Phys. Commun.* **184**, 1234 (2013).
- [66] Z. He, Review of the shockley–ramo theorem and its application in semiconductor gamma-ray detectors, *Nucl. Instrum. Methods Phys. Res. A* **463**, 250 (2001).
- [67] As a simpler example, here, we consider the AC Stark shift in the case where the Hamiltonian can be written as $H = \frac{\hbar\Omega_1}{2}s_x^B + 2Js_z^B|2^A\rangle\langle 2^A|$, where the notations are the same as in the main text. We denote $|n_z^B(0)\rangle$ as the initial state of qubit B. When the initial state of qubit A is $|1^A\rangle$, the state becomes $|1^A\rangle R_x^B(\Omega_1 t_p) |n_z^B(0)\rangle$ after time t_p . When the initial state of qubit A is $|2^A\rangle$, the state becomes $|2^A\rangle R_{(\cos v, 0, \sin v)}^B(\sqrt{\Omega_1^2 + (\frac{4J}{\hbar})^2} t_p) |n_z^B(0)\rangle$ with $v = \arctan \frac{4J}{\hbar\Omega_1}$ after time t_p . Here, $R_{\square}^{\circ}(\Xi)$ is the rotation operator for the spin state of qubit $\circ = A, B$ with angle Ξ along the \square axis.
- [68] J. Zhang, J. Vala, S. Sastry, and K. B. Whaley, Exact two-qubit universal quantum circuit, *Phys. Rev. Lett.* **91**, 027903 (2003).
- [69] M. J. Bremner, C. M. Dawson, J. L. Dodd, A. Gilchrist, A. W. Harrow, D. Mortimer, M. A. Nielsen, and T. J. Osborne, Practical scheme for quantum computation with any two-qubit entangling gate, *Phys. Rev. Lett.* **89**, 247902 (2002).
- [70] Y. P. Monarkha and S. S. Sokolov, Decay rate of the excited surface electron states on liquid helium, *Low Temp. Phys.* **32**, 970 (2006).
- [71] R. Cabrera and W. E. Baylis, Average fidelity in n-qubit systems, *Phys. Lett. A* **368**, 25 (2007).
- [72] T. P. Bertelli, E. C. Passamani, C. Larica, V. P. Nascimento, A. Y. Takeuchi, and M. S. Pessoa, Ferromagnetic properties of fcc gd thin films, *J. Appl. Phys.* **117**, 203904 (2015).